

Conceptual Design Report of a Regional Airliner Jet

Academic responsible: Dr. Errikos Levis & Dr. Robert Hewson
Department: Department of Aeronautics
Course: MEng in Aeronautics
Module: AERO60002
Academic year: 2022/2023
Student: Amelia Samuel - 01873907
Aryaa Desai - 01846886
Avish (Ave) Madhow - 01951532
Chris Ziyi Yao - 01908293
Stephen Cao - 01854692
YiChen You - 01863827
Group: 01
Date: 02/12/2022

Department of Aeronautics
South Kensington Campus
Imperial College London
London SW7 2AZ
U.K.



Abstract

This report details the conceptual design and sizing of a regional jet aircraft aiming to carry 5 crew members and 90 passengers over a 3-leg mission spanning from Wellington to Christchurch to Hamilton. From initial sizing parameters of $C_{L_{max}} = 2.00$, $(T/W)_0 = 0.289$ and $(W/S)_0 = 4448 \text{ N/m}^2$, the aircraft wing, tailplane, propulsion system, fuselage, systems layout, weight and balance, undercarriage, aerodynamics, stability and performance were determined to meet the design requirements. These were sized and designed using existing empirical methods as well as iterative approaches. From empirical weight estimation, the aircraft was found to be 4.57% lighter than the initial sizing MTOW of 45887.9 kg. Stability and Trim analysis of the aircraft showed that the aircraft would be stable in the worst-case scenario of flight with a static margin value ranging from 11.43% to 12.59%. For field performance, while the takeoff distance requirements are within the designed requirements, the landing distance required was an overestimation of the design constraint. The maximum range of the aircraft when fully loaded was found to be $2.41 \times 10^3 \text{ km}$.

Contents

List of Symbols	ii
List of Figures	iv
List of Tables	v
1 Revisions from Initial Sizing	1
2 Wing Design	2
2.1 Wing Vertical Location	2
2.2 Aerofoil Selection	2
2.3 Wing Planform Design	3
2.3.1 Wing Planform	3
2.3.2 Wing Sweep Angles (Λ)	4
2.3.3 Taper Ratio (λ)	4
2.3.4 Twist (ϵ)	5
2.3.5 Dihedral (Γ)	6
2.3.6 Wing Incidence	6
2.4 Summary of Wing Planform Design	6
2.5 High Lift Devices (HLDs)	7
3 Tailplane Design (V_{HT} & V_{VT})	8
3.1 Volume Coefficient	8
3.2 Aspect Ratio	8
3.3 Tail Arm (l_{HT} & l_{VT}) & Tail Planform	8
3.4 Sweep Angle (λ_{HT} & λ_{VT})	10
3.5 Taper Ratio (λ_{HT} & λ_{VT})	10
3.6 Aerofoil Selection	10
3.7 Twist (ϵ_{HT}) & Dihedral (Λ_{HT})	11
3.8 Summary of Tailplane Parameters	11
4 Control Surface Design	12
4.1 Aileron Design	12
4.2 Spoiler Design	12
4.3 Rudder Design	13
4.4 Elevator Design	13
5 Fuselage Design	14
5.1 Cabin Design	14
5.2 Empennage Design	16
5.3 Cockpit Design	16
6 Propulsion System Design	17
6.1 Propulsion Selection	17
6.2 Engine Installation	18
6.3 Engine Selection	18
6.4 Capture Area and Inlet Sizing	19
6.5 Nozzle Geometry	19
6.6 Engine Integration	19
7 Structural Layout	20
7.1 Fuselage Structure	20
7.2 Wing and Tailplane Structure	20
7.3 Dynamic Loading Considerations	20
7.4 Material Selection	20

8 Aircraft Systems Layout	20
8.1 Fuel System	20
8.2 Hydraulics and Pneumatic	21
8.3 Electrical System	22
8.4 De-Icing System	22
8.5 Avionics	23
9 Weight and Balance	23
9.1 Weight Estimation	23
9.2 Balance Estimation	23
10 Undercarriage Design	25
10.1 Layout	25
10.2 Positioning	25
10.3 Tyre Choice and Sizing	27
10.4 Shock Absorber Design	28
11 Aerodynamics - Drag Estimations	28
11.1 Parasite Drag (Zero-Lift Drag)	28
11.1.1 Rapid Drag Estimation Method	28
11.1.2 Component Buildup Method	29
11.2 Total Drag Coefficient	31
11.3 Total Trimmed Drag	31
12 Stability and Trim	32
12.1 Stability	32
12.1.1 Longitudinal Static Stability	32
12.1.2 Directional stability	34
12.1.3 Trim analysis	34
13 Aircraft Performance	36
13.1 Take-off distance	36
13.2 Balanced Field Length	37
13.3 Landing Distance	37
13.4 Mission Performance	38
13.5 Point Performance	39
14 Evaluation of Conceptual Design	40
A Appendix: Three View Drawing	43
B Appendix: Poster Design	45

List of Symbols

d_f	Maximum Diameter of the Fuselage
AR	Aspect Ratio
$b_a, b, b_{ht}, b_{vt}, b_i, b_o, b_s, b_r$	Span of Aileron, Wing, Horizontal Stabilizer, Vertical Stabilizer, Inboard, Outboard, Spoiler, Rudder
$c_a, c, c_{ht}, c_{vt}, c_i, c_o, c_s, c_r$	Chord Length of Aileron, Wing, Horizontal Stabilizer, Vertical Stabilizer, Inboard, Outboard, Spoiler, Rudder
$\delta_{a_{max}}, \delta_{s_{max}}, \delta_r, \delta_E$	Maximum Aileron, Spoiler, Rudder Deflection, Elevator Deflection
$S_a, S_{ref}, S_{ht}, S_{vt}, S_s, S_r, S_W, S_{flapped}$	Area of Aileron, Reference Wing, Horizontal Stabilizer, Vertical Stabilizer, Spoiler, Rudder, Wing, Flaps
$C_{L_{Design}}, C_{L_{max}}, C_{L_c}, C_{L_W}, C_{L_h}$	Lift Coefficient; Design, Maximum 3D, Cruise, Wing, Tailplane
$C_{L_\alpha}, C_{L_\alpha W}, C_{L_\alpha h}, C_{L_{\delta_E}}$	Lift-Curve Slope; General, Wing, Tailplane, Elevator
$\alpha, \alpha_{trim}, \alpha_{0W}, \alpha_{0h}$	AoA; General, Trim, Zero-lift wing, Zero-lift Tailplane
x_{CG}, z_{CG}, y_{CG}	Centre of Gravity; x-direction, z-direction, y-direction
λ	Taper Ratio
$\Lambda_{c/4}$	Quarter-chord sweep
Λ_{LE}	Leading Edge sweep
Λ_{TE}	Trailing Edge sweep
$c_{tip}, c_{root}, \bar{c}$	Tip, Root and Mean chord lengths
\bar{Y}	Spanwise Position of mean chord
ϵ	Twist angle
Γ	Dihedral angle
i_w, i_h	Wing Setting Angle, Tail Setting Angle
$M, M_{cruise}, M_{DD}, M_{crit}$	Mach Number; General, Cruise, Drag-Divergence, Critical
$C_{M_{\alpha_f}}$	Fuselage Pitching Moment Derivative
x_{acW}, x_{ach}	Aerodynamic Centre of Wing, Tailplane
x_{np}	Neutral Point
$d\epsilon/d\alpha$	Downwash derivative
$dC_M/d\alpha$	Pitching moment derivative
$C_{M_{CG}}$	Wing zero-lift pitching moment
q	Dynamic Pressure
K_n	Static Margin
η, η_h, η_T	Shock Absorber efficiency, Tailplane efficiency, Tyre efficiency
V_v	Touch-down sink speed
N_g	Gear load factor
C_D	Drag Coefficient
C_{D_0}	Zero-lift drag coefficient
C_{D_i}	Induced drag coefficient
S_{Wet}	Wetted Area
C_f	Skin Friction coefficient
Q	Interference factor
S_g	Ground Rolling Distance
S_r	Rotation Distance
S_{tr}	Transition Distance
h_{obs}	Obstacle height
S_{TO}	Total Takeoff Distance
BFL	Balanced Field Length
σ	Relative Density
SFC	Specific Fuel Consumption
S_A	Total Landing Distance
S_B	Ground Braking Distance
S_F	Flare Distance
γ	Climb Gradient
V_s	Stall Speed
D_{Oleo}	Oleo diameter
L_{Oleo}	Oleo length
c'	Specific Fuel Consumption Factor
L_f	Length of fuselage
w_f	Maximum fuselage width
K_f	Fuselage and engine nacelle moment factor

List of Figures

1	Mission Profile	1
2	Constraint Diagram	1
3	Influence of the sweep on the lift distribution and the stall behavior	5
4	Planform dimensions	7
5	X and Z Position of the Tailplane aft Wing, background plot based on [1]	9
6	Design Point of Horizontal & Vertical Tailplane, based on the plot of [2]	10
7	Vertical Tailplane Dimensions	11
8	Horizontal Tailplane Dimensions	11
9	Historical Guidelines for aileron span and chord ratios	12
10	Operation of a spoiler	13
11	Top View of the Fuselage Layout	15
12	Front View of the Fuselage Layout	15
13	Side View of the Fuselage Layout	16
14	Top view of cockpit	17
15	Side View and Minimum Viewing Distance from the Cockpit	17
16	Layout of Pitot Inlet	19
17	Wing Fuel System. Red area indicates the surge tank.	21
18	Basic Hydraulic System (drawing not indicative of final design)	22
19	Basic Pneumatic Diagram	22
20	Basic Diagram of the Electrical Systems. Lines in green are Used During Primary System Failure.	23
21	CG envelope for specified load cases	25
22	Diagram showing the origin defined for overturn, vertical CG angle and clearance calculations	26
23	Graph showing the lines drawn to calculate the overturn angle and vertical CG angle for the aftmost CG case. This was repeated for the foremost CG	26
24	Graph showing how the engine clearance was determined	27
25	Calculation of ACN values using COMFAA	27
26	Variation of K_f with relative location of wing and body	33
27	Iterative $C_{M_{CG}}$ vs C_L for different values of α_{trim} , i_h and i_w	35
28	Range in range with different layout weight	39
29	Specific Excess Power plot with the climb rate measured in ft/min	39
30	Front View	43
31	Side View	43
32	Top View	44
33	Initial Design Poster	45

List of Tables

1	Summary of Shortlisted Aerofoil Data at $C_{L_{cruise}}$ at Closest Possible Cruise Reynolds Number on Database	3
2	Summary of Shortlisted Aerofoil Data	3
3	Typical Dihedral angle for specific wing positions	6
4	Summary of wing planform parameters	7
5	Summary of HLD sizing parameters	8
6	Comparison of results calculated by 2 methods	9
7	Summary of Tailplane Parameters	11
8	Summary of aileron sizing parameters for wing semi-span	12
9	Summary of spoiler sizing parameters for wing semi-span	13
10	Summary of rudder parameters	13
11	Summary of elevator parameters	14
12	Design Parameters of the Fuselage	16
13	Shortlisted Engine with Length, Height and Weight Adjusted	18
14	Engine Property & Nacelle Geometry	19
15	Fuel Distribution across the aircraft. [†] Surge tank not accounted for in volume/weight summary	21
16	Breakdown of Weight and Balance estimations. [†] y_{CG} for furnishing was estimated to be 2.8 ft	24
17	CG locations based on loading cases	24
18	Table comparing overturn angle, vertical centre of gravity angle and load on nose gear for the aftmost and foremost centre of gravity positions	25
19	Table summarising the final x-position of the main gear, nose gear and centre of gravity .	26
20	Table displaying the calculated loads per wheel and subsequent tyre choices. RL = Rated Load, RBL = Rated Braking Load, P = Pressure, R = Radius, A = Area	27
21	Nose and Main gear specifications. L = Length, δ = deflection	28
22	Drag from aircraft components in different mission stages	29
23	Summary of skin-friction coefficient C_f	30
24	Drag from aircraft components in different mission stages	30
25	Summary of Miscellaneous Drag Coefficient $C_{D,misc}$	31
26	Summary of Wave Drag Coefficient in Cruise	31
27	Summary of Trimmed Drag	32
28	Summary of Total Drag C_D during Takeoff and Landing	32
29	Summary of K_n analysis in power-on configuration	34
30	Summary of K_n analysis in power-on configuration	35
31	Breakdown of takeoff parameters	36
32	Breakdown of BFL parameters	37
33	Breakdown of landing parameters	38
34	Brequet Range/Endurance Updated	38

1 Revisions from Initial Sizing

The report goes over the development of a conceptual regional passenger aircraft flying in New Zealand. The aircraft should seat 90 passengers, 3 cabin crews and 2 pilots all in compliance with FAR 25 regulations. The mission profile is shown in Figure[1].

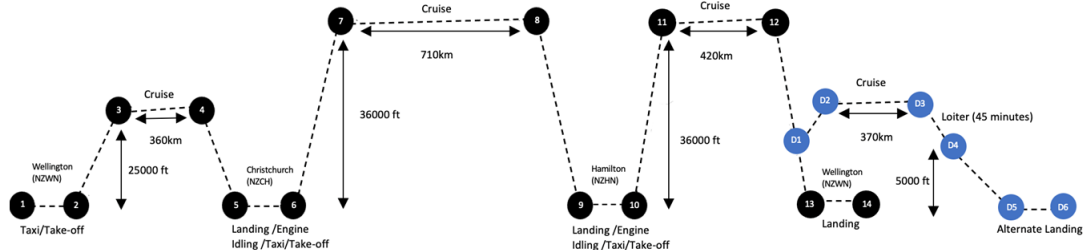


Figure 1: Mission Profile

A baseline configuration of a low wing, conventional tails, underwing podded nacelle and a tricycle undercarriage was selected. A constraint diagram with a selected design was chosen and shown in APPENDIX A. However, the design point in Figure[2] was not the first design point, rather the point was reassessed after the constraint diagram had been updated after feedback. Changes made to the initial conception were adjusting the vast overestimation of the aircraft payload, weight fraction was made more realistic given the mission profile and correcting, mainly the $(L/D)_{max}$ value to an ambitious value. This resulted in a thrust-to-weight ratio at sea level $(T/W)_0$ of 0.289 and a wing loading W_0/S of 4448 N/m^2 . The empty weight was estimated to be $2.340 \times 10^4 \text{ kg}$, and passenger and crew member were estimated to be 75 kg with each passenger carrying a maximum of 23 kg of luggage each summing to a payload weight of 9285 kg. The weight fraction was estimated to be 29.0% of the maximum takeoff weight (MTOW) resulting in a minimum fuel weight of $1.380 \times 10^4 \text{ kg}$. The MTOW of the aircraft comes to $4.589 \times 10^4 \text{ kg}$; so the required thrust turns to 130 kN with the wing reference area of 101.205 m^2 . The target $C_{L_{max}}$ values for takeoff, clean configuration and landing were adjusted to 2.10, 2.00 and 2.40 respectively with a high but reduced value of $(L/D)_{max} = 17.20$.

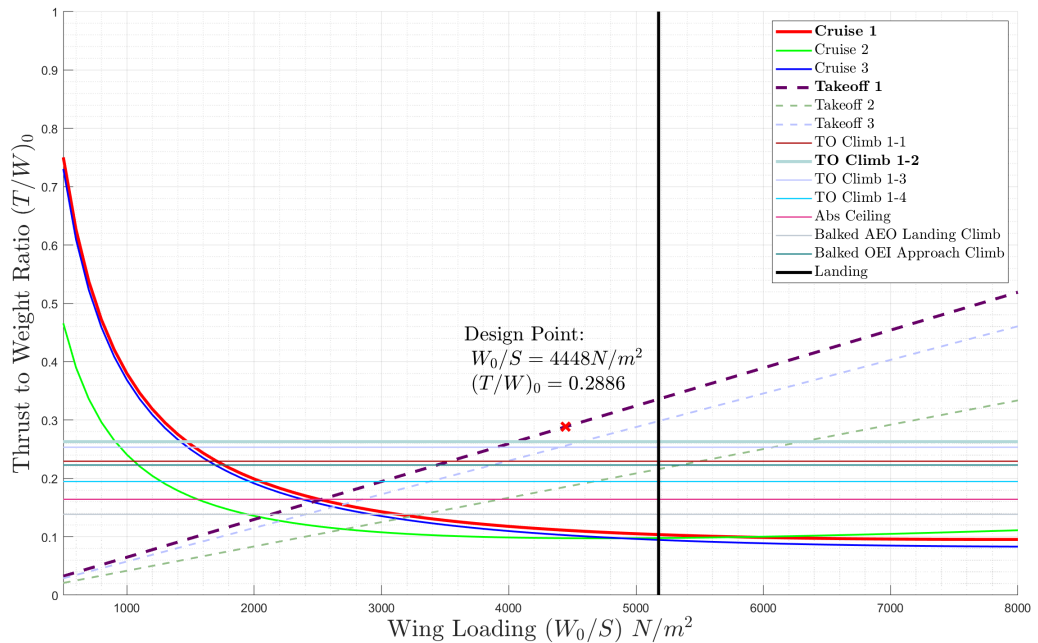


Figure 2: Constraint Diagram

2 Wing Design

2.1 Wing Vertical Location

A low wing configuration was chosen mainly for the landing-gear stowage as the retraction system could be placed inside the wing, which makes the landing gear lighter. It thus requires less space inside the wing for a retraction system and would further make the wing structure lighter. A low-mounted wing would also have less induced drag and generate less down-wash on the tail, improving the latter's effectiveness in flight. However, the wing has less contribution to the aircraft dihedral effect, thus the aircraft is laterally dynamically less stable.

2.2 Aerofoil Selection

Selecting an appropriate aerofoil is one of the key parts of designing a wing, as it impacts both the aerodynamics of the aircraft and also has significant contribution towards the overall structural weight of the aircraft. The method used to select the most appropriate aerofoil was done based on the assumption that a reliable database of a selection of different aerofoils existed and from it, the best one which matched this project's requirements was selected. The NACA 6-series aerofoils were the best starting point due to being the most efficient in the mission profile given. The 6-series aerofoils were designed to maintain a laminar flow over a large part of the chord, thus maintaining a lower minimum drag coefficient compared with four- and five- series aerofoils [3].

Another big advantage of the 6-series aerofoils is its typical variations of the drag coefficient with the lift coefficient. Theoretically, the value of minimum drag does not change for a limited range of C_l . This is important as it implies that the pilot can stay at the lowest drag point whilst changing the angle of attack. This situation models the cruising flight conditions since the aircraft weight is reduced as the fuel is burned. Hence, the pilot can bring the aircraft nose down (decrease the angle of attack) without being worried about an increase in the aircraft drag. Therefore it is possible to keep the engine throttle low during cruising flight.

After this had been determined, a key selection factor was the aerofoil's design lift coefficient, $C_{l_{Design}}$, in cruise conditions. This was found by equating lift and weight and determining the aircraft's design lift coefficient C_{L_c} first. This equation however assumes that all of the lift is generated by the wings without taking into account the fuselage as a lifting surface, so a correction factor of dividing by 0.95 must be applied resulting in the wing coefficient of lift, C_{L_w} which is reliable as it was determined by professional CFD analysis [4]. Finally, in order to determine the aerofoil's design lift coefficient $C_{l_{Design}}$ during the cruise, an additional correction factor of division by 0.9 has to be applied. The reason being is as the wing has not been designed yet, an approximate solution that would account for the lack of sweep angle, dihedral and an assumption of wing span of infinity must be applied. The calculations are shown below in equation (1), where the final value is obtained to be $C_{L_{Design}} = 0.4799$.

$$C_{L_c} = \frac{2W_{avg}}{\rho V_C^2 S} \quad C_{L_{cw}} = \frac{C_{L_c}}{0.95} \quad C_{L_{Design}} = \frac{C_{L_{cw}}}{0.90} \quad (1)$$

The next step was to calculate the wing aerofoil maximum lift coefficient $C_{l_{max}}$ which was calculated in a similar way to that above, where the equation for $C_{l_{Max}}$ is shown below (2) with the velocity is the stall velocity and the weight is the takeoff weight and ρ is that at the sea level.

$$C_{L_{max}} = \frac{2W_{TO}}{\rho_0 V_s^2 S} \quad C_{L_{Max_W}} = \frac{C_{L_{max}}}{0.95} \quad C_{L_{max_{gross}}} = \frac{C_{L_{Max_W}}}{0.90} \quad (2)$$

Finally, the wing aerofoil maximum lift coefficient $C_{L_{max}}$ can be calculated using equation (3) where $\Delta C_{L_{HLD}}$ was empirically given as 1.1, a value typical for Fowler flaps was chosen as the high lift device on this aircraft.

$$C_{L_{max}} = C_{L_{max_{gross}}} - \Delta C_{L_{HLD}} \quad (3)$$

$C_{L_{max}}$ then becomes 1.259. These two factors were then used to shortlist five aerofoils with the following characteristics shown in the table.

Table 1: Summary of Shortlisted Aerofoil Data at $C_{L_{cruise}}$ at Closest Possible Cruise Reynolds Number on Database

Aerofoil	$(\frac{L}{D})_{max}$	$C_{l_{Design}}$	$\frac{t}{c}$	$C_{d_{cruise}}$
NACA 63 ₁ -212	91.9	0.6013	0.12	0.00654
NACA 64 ₁ -212	91.2	0.5971	0.12	0.00655
NACA 65 ₁ -212	87.8	0.5383	0.12	0.00613
NACA 64 ₁ -215	99.2	0.7180	0.15	0.00724
NACA 64 ₁ -112	76.6	0.4836	0.12	0.00631

Table 2: Summary of Shortlisted Aerofoil Data

Aerofoil	C_{M_0}	$\alpha(^{\circ}) @ C_{l_{max}}$	C_d	$C_{l_{max}}$
NACA 63 ₁ -212	-0.0398	14.750	0.00555	1.3204
NACA 64 ₁ -212	-0.0398	13.500	0.00556	1.2875
NACA 65 ₁ -212	-0.0401	12.000	0.00555	1.1813
NACA 64 ₁ -215	-0.0383	16.750	0.00629	1.3288
NACA 64 ₁ -112	-0.0219	13.750	0.00555	1.2230

From this point onward, the value of $C_{l_{Design}}$ at which $(\frac{L}{D})_{max}$ occurs at a relatively high value, was chosen due to highest fuel efficiency. The desired aerofoil also had to have one of the lowest values of C_{M_0} which is important since it stabilizes the flight if the angle of attack is disturbed by a gust longitudinally. The aerofoil also had to have a value of $C_{l_{Max}}$ within the range that was desired as mentioned above. The coefficient of drag, C_d is also relatively small out of the five for this aerofoil. Finally, a thickness-to-chord ratio of 12 % was deemed sensible as it was not too thin to not be able to store fuel and be structurally compromised for such a large aircraft. The NACA 64₁-212 aerofoil was therefore chosen.

2.3 Wing Planform Design

2.3.1 Wing Planform

The dimensions of the trapezoidal planform of the wing could be found using the following relations. The wing span, b , is a function of the aspect ratio (AR) and wing reference area and is calculated using $b = \sqrt{ARS_{ref}}$ to yield a value of $b = 28.45$ m.

The tip and root chords, c_{tip} and c_{root} , are calculated using the following equations, being coupled with the taper ratio calculated in section 2.3.3, and found to be 1.36 m and 5.75 m respectively.

$$c_{root} = \frac{2S_{ref}}{b(1 + \lambda)} \quad (4)$$

$$c_{tip} = \lambda c_{root} \quad (5)$$

Furthermore, the mean aerodynamic chord (\bar{c}) and its spanwise location (\bar{Y}) from the wing root could be found using the following equations. These were calculated to be $\bar{c} = 4.01$ m and $\bar{Y} = 5.65$ m

$$\bar{c} = \frac{2}{3}c_{root} \left(\frac{1 + \lambda + \lambda^2}{1 + \lambda} \right) \quad (6)$$

$$\bar{Y} = \left(\frac{b}{6} \right) \left(\frac{1 + 2\lambda}{1 + \lambda} \right) \quad (7)$$

The final parameter required to size the planform was the sweep which would be detailed in the upcoming section.

2.3.2 Wing Sweep Angles (Λ)

Aft sweep is needed at high subsonic speed flight to improve the wing aerodynamic features such as lift, drag and pitching moment by delaying the onset compressibility effects which give rise to drag divergence. Aft swept wings are also inherently aeroelastically stable. Sweep is related to both the thickness to chord ratio, t/c , set to 0.12 for the selected aerofoil and the drag divergence Mach number, M_{DD} , which in this case was set to the maximum cruise speed Mach number of 0.69. These parameters could be related together using the following equation [2]:

$$\frac{t}{c} = \frac{0.30}{M_{DD}} [(M_{DD}\cos(\Lambda_{c/4}))^{-1} - M_{DD}\cos(\Lambda_{c/4})]^{\frac{1}{3}} \left[1 - \left(\frac{5 + (M_{DD}\cos(\Lambda_{c/4}))^2}{5 + (1 - 0.25C_{l_{Design}}(\cos(\Lambda_{c/4}))^{-2})^2} \right)^{3.5} \right]^{\frac{2}{3}} \quad (8)$$

An iterative method was used to solve the equation, the quarter-chord sweep was found to be $\Lambda_{c/4} = 22.36^\circ$ with $C_{L_{Design}} = 0.59$. Further to that, the leading edge sweep, required to reduce compressibility effects and thus aerodynamic drag at the onset of supersonic regime, and trailing edge sweep, serving a similar purpose by reducing sonic boom intensity, can be calculated using the following equations, based on the geometry of the trapezoidal planform:

$$\Lambda_{TE} = \tan^{-1} \left(\frac{c_{root} - c_{tip}}{b} \right) \quad (9)$$

$$\tan(\Lambda_{LE}) = \tan(\Lambda_{c/4}) + \frac{(1 - \lambda)}{AR(1 + \lambda)} \quad (10)$$

As seen above, these are coupled with the wing chord dimensions, aspect ratio and taper ratio and could be calculated to yield $\Lambda_{LE} = 27.40^\circ$ and $\Lambda_{TE} = 11.83^\circ$ respectively.

Several drawbacks would be brought by the sweep angle. It changes the direction of the bound vortices, re-directing the flow towards the tip of the wing at high incidences. The vorticity pushes pressure downstream which leads to the highest pressure drag at the centre of the wing due to the formation of a suction peak. The boundary layer would develop from the root to the tip and reach its biggest thickness and the suction peak at the tips due to adverse pressure gradient, leading to a trend of tip flow separation and thus stall. To mitigate these impacts, taper ratio and twist angles are introduced.

2.3.3 Taper Ratio (λ)

Wing taper ratio λ , defined as the ratio of the tip chord, c_{tip} , to the centre-line root chord, c_{root} , can favourably impact the aerodynamic and structural performance of the aircraft. Aerodynamically, tapering improves lift distribution and minimises lift-induced drag by simulating an elliptic lift distribution as far as possible when applied to a trapezoidal wing [5]. Structurally, the taper will reduce the weight of the wings since their respective centres of gravity will move towards the fuselage centre-line, lowering the bending moment at the roots. Furthermore, the wing mass moment of inertia about the longitudinal axis will be reduced. Consequently, this will improve the aircraft lateral control [5]. However, if overdone, tapering can increase the manufacturing costs of wings, since wing ribs will have different shapes and sizes. The lateral stability will also be impacted since tapering usually generates some degree of sweeping. Thus efficiency could be compromised given that the aircraft wings will be swept back, already countering the positive rolling moment.

$$\lambda = \frac{c_{tip}}{c_{root}} \quad (11)$$

An un-tapered, rectangular wing has a significant aerodynamic disadvantage due to the large chord at the wing tip resulting in about 7% higher induced drag than a tapered one. Typically, $\lambda = 0.45$ for unswept wings to achieve an approximate elliptical lift distribution, having an induced drag which is then less than 1% higher than the induced drag of the wing with the elliptical lift distribution. Since the designed aircraft wing is swept, however, the lift distribution in the vicinity of the wing tip tends to be higher as shown below.

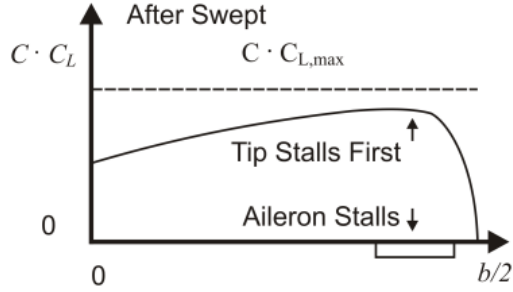


Figure 3: Influence of the sweep on the lift distribution and the stall behavior

Thus, to get as close as possible to an elliptic lift distribution, λ must be smaller than 0.45. According to [2], this taper ratio, coupled with $\Lambda_{c/4}$ can be calculated using the following relation:

$$\lambda_{opt} = 0.45e^{-0.036\Lambda_{c/4}} \quad (12)$$

This gives a value of $\lambda_{opt} = 0.2$. However, this value falls short of the expected range of 0.3 to 0.5 for commercial airliners. Thus a slightly larger value of $\lambda_{opt} = 0.236$ is chosen, which aligns with data from similar regional jetliners such as the BOEING 757 [4].

2.3.4 Twist (ϵ)

Tapering will result in a lower Reynolds number at the wing tip as well as a lower tip induced downwash angle. Both of these will lower the angle of attack at which stall occurs. Thus the tip may stall before the root. This can prove unfavourable from the viewpoint of lateral stability and lateral control as it can induce an abrupt roll and loss of control that can lead to undesirable spin. As such, aircraft wings often have a degree of twist along the span, such the angle-of-incidence(AOI) of the tip airfoil is different from the root airfoil. Twist is used to prevent wing tip stall and revise the lift distribution to an elliptic distribution. Total effective twist, ϵ , is the sum of geometric and aerodynamic washout, ϵ and ϵ respectively.

$$\epsilon = \epsilon_G + \epsilon_A \quad (13)$$

The aerodynamic washout can be simplified in terms of stall angles of attacks for the wing root and tip airfoils, which can be obtained from the lift coefficient distribution of the airfoil.

$$\epsilon_A = \alpha_{stall,root} - \alpha_{stall,tip} \quad (14)$$

In the case of this aircraft, the effective aerodynamic washout can be deemed to be negligible given the fact that the same airfoil section is used throughout the wing. Also, modelling the flow field over the wing at stall is deemed too complicated for the simplicity of the current approach [4]. Thus, only geometric twist is applied and geometrically it can be seen that this is simply the difference of wing setting angle (i_w) between the root and tip of the wing:

$$\epsilon_G = i_{w,tip} - i_{w,root} \quad (15)$$

A noteworthy criterion in deciding twist comes from the fact that the twist angle must not be such high that it results in a negative lift in the outer wing portions [5]. This criterion can be formulated as follows, knowing that every section has zero-lift angle of attack, α_o :

$$|\epsilon| + i_w \geq |\alpha_o| \quad (16)$$

Typical geometric twist angles range from -1° to -4° . At this stage in the conceptual design, multiple factors such as the wing incidence have not yet been finalised and thus calculating a twist angle is not feasible. Therefore a reasonable estimate of $\epsilon = -3^\circ$, which provides decent stall characteristics, is made by looking at the washout of similar AIRBUS and BOEING commuter jets [6].

2.3.5 Dihedral (Γ)

A low-wing configuration has a larger tendency to experience sideslip compared to other configurations, making it less laterally stable. This occurs because the fuselage distorts the sideflow such that the windward wing sees a smaller angle of attack near the root, leading to a positive rolling moment. This implies that a dihedral wing angle is needed to improve lateral stability to maintain wings-level equilibrium if the aircraft is disturbed [5]. However wing sweep must also be considered given that a swept wing closest to sideslip direction will experience a higher velocity normal to the wing's leading edge than the wing away from the sideslip. Thus, lift is generated on the wing toward the sideslip and a negative rolling moment arises, contributing towards lateral stability. It should hence be noted that a combination of sweep and dihedral could produce excessive lateral stability, compromising roll manoeuvre performance.

Table 3: Typical Dihedral angle for specific wing positions

	Wing Position		
	Low	Mid	High
Unswept(Civil)	5 to 7	2 to 4	0 to 2
Subsonic swept wing	3 to 7	-2 to 2	-5 to 5
Supersonic swept wing	0 to 2	-5 to 0	-5 to 5

Having a subsonic swept wing, this aircraft requires would theoretically require a dihedral angle between 3° and 7° [7] according to Table 3. From [7], it is stated 10° of sweep achieves roughly as much as 1° dihedral. Factoring in the calculated quarter-chord sweep angle of 22.36° , this implies that about 2.236° of equivalent dihedral is achieved to counter rolling moment already. From a chosen intermediate value of $\Gamma = 5^\circ$ from Table 3, as the most common choice for similar aircraft to the one proposed, subtracting 2.236° from it yields a final choice of $\Gamma_{eff} = 2.8^\circ$ for effective wing dihedral.

2.3.6 Wing Incidence

The wing angle of incidence, i_w , is defined as the angle between the root wing chord and a horizontal reference line on the fuselage, typically the centre-line of the fuselage, defined parallel to the cabin floor. This is chosen primarily to minimise drag in cruise flight and also allow the fuselage to generate enough lift to keep the cabin floor horizontal. As such, the fuselage angle of attack in trim flight should be almost zero to limit drag and prevent sloped cabin. On this basis, i_w can be found from the C_L vs α graph of the selected aerofoil. This corresponds to the angle of incidence matching the $C_{L_{Design}}$ of the aerofoil. This yields a value of $i_w = 2.5^\circ$. This value is, however, refined and calculated when considering the trimmability of the aircraft to yield a design point value of $i_w = 0.5^\circ$.

2.4 Summary of Wing Planform Design

Figure 4 illustrates the parameters of the semi-wing planform. Table 4 summarises the main parameters and dimensions of the wing planform.

Table 4: Summary of wing planform parameters

Parameter	Value
AR	8
S_{ref} (m^2)	101.21
b (m)	28.45
c_{tip} (m)	1.36
c_{root} (m)	5.75
\bar{c} (m)	4.01
\bar{Y} (m)	5.65
λ	0.236
$\Lambda_{c/4}$ ($^\circ$)	22.36
Λ_{LE} ($^\circ$)	27.40
Λ_{TE} ($^\circ$)	11.83
ϵ ($^\circ$)	-3
Γ ($^\circ$)	+2.8
i_w ($^\circ$)	0.5
M_{crit_w}	0.65

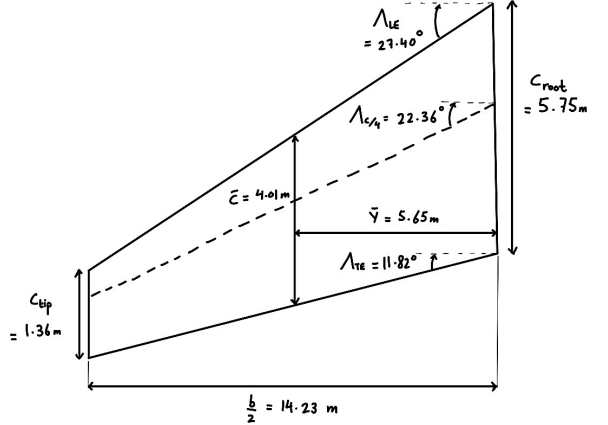


Figure 4: Planform dimensions

2.5 High Lift Devices (HLDs)

The aircraft wing is required to achieve higher lift during takeoff and landing operations as the airspeed is very low compared with cruising speed, leading to the wing needing to produce a larger lift coefficient. High lift devices are thus employed to increase $C_{L_{max}}$ at these segments by changing the aerofoil section's and wing's camber.

Fowler flaps are chosen as trailing edge devices because they increase the exposed area of the wing, thus generating a further increase in lift. These have a special mechanism that when deployed, not only deflects downward but also translates or tracks to the trailing edge of the wing. As such, the lift can be increased without a disproportionate increase in drag. Fowler flaps are also less complex than double or triple-slotted flaps which would be more costly and challenging to manufacture and lead to an increase in wing weight. Leading edge slats are also chosen primarily to modify the pressure distribution over the top surface of the wing. Being highly cambered, the slat itself has a much lower pressure over its top surface. However, this flow interaction results in a higher pressure over the top surface of the main wing body [5]. Thus it delays flow separation over the wing and mitigates to some extent the otherwise strong adverse pressure gradient that would exist over the main wing section. Consequently, the lift coefficient is increased with no significant increase in drag.

The estimate for the maximum lift coefficient to correct for high-lift devices is as follows:

$$\Delta C_{L_{max}} = 0.9 \Delta C_{l_{max}} \left(\frac{S_{flapped}}{S_{ref}} \right) \cos(\Lambda_{HL}) \quad (17)$$

, whereby $\Delta C_{l_{max}}$ is the sectional change in lift coefficient generated by the high lift devices, Λ_{HL} is the sweep angle of the flap hinge, $S_{flapped}$ is the area of the high lift device and 0.9 represents a knock-down factor to correct for three-dimensional effects of real flow. $\Delta C_{l_{max}}$ can be found using empirical relations.

For Fowler flaps, $\Delta C_{l_{max,flap}} = 1.3 \frac{c'}{c}$ [8], where $\frac{c'}{c}$ is the ratio of effective chord due to an extended flap to the ratio of aerofoil. Typically, for fowler flaps 30% of the wing chord is assigned as the flap chord length, which yields a value of $\Delta C_{l_{max,flap}} = 1.69$. For leading edge slats, $\Delta C_{l_{max,slat}} = 0.4 \frac{c'}{c}$. Typically, 15 to 17.5% of the wing chord [4] is assigned as the slat chord length. 17.5% is chosen to size the slat for maximum lift generation, yielding a value of $\Delta C_{l_{max,slat}} = 0.47$.

In terms of span, on the basis that the aileron occupies about 30% of the wing span, flaps typically extend over 65% to 80% of the exposed semi-span, with the outboard sections reserved for ailerons. The resultant flapped area ratios are generally in the range of 55% to 70% of the reference area [5]. As such, a value of $\left(\frac{S_{slats}}{S_{ref}} \right) = 0.70$ is chosen to size the slats first. This yields a $\Delta C_{L_{max,slats}} = 0.263$ using $\Lambda_{HL} = \Lambda_{LE} = 27.40^\circ$. Subsequently, noting that, at landing, $C_{L_{max,landing}} = 2.40$ from initial sizing and that

clean configuration $C_{L_{max}} = 1.2875$ from aerofoil data, the lift contribution from the high lift devices is $C_{L_{max,HLD}} = 1.18$. As such, this implies that $\Delta C_{L_{max,flaps}} = C_{L_{max,HLD}} - \Delta C_{L_{max,slats}} = 0.840$ Using this, the value of $\left(\frac{S_{flaps}}{S_{ref}}\right)$ can be found to be 0.57.

The slats are sized at 80% of the exposed wing semi-span, yielding a slat semi-span of 11.38 m, which provides a leeway clearance of 1.42 m from the fuselage and wingtip to place the slat on the wing. The $\left(\frac{S_{flaps}}{S_{ref}}\right)$ ratio of the flaps corresponds to a flap size at 58% of the exposed wing semi-span, yielding a flap semi-span of 8.29 m, providing enough space to place the aileron as well on the trailing edge of the wing. The results of this section's sizing are summarised in Table 5 below:

Table 5: Summary of HLD sizing parameters

HLD	$\frac{c'}{c}$	$\left(\frac{S_{flapped}}{S_{ref}}\right)$	Semi-Span(m)	% of $\frac{b}{2}$	$\Delta C_{L_{max}}$
LE Slats	1.18	0.70	11.38	80	0.263
Fowler Flaps	1.30	0.57	8.29	58	0.840

3 Tailplane Design (V_{HT} & V_{VT})

3.1 Volume Coefficient

The initial Volume Coefficients (V_{HT} & V_{VT}) for both horizontal and vertical tails were selected according to the empirical regression data as $V_{HT} \approx 1.0$ & $V_{VT} \approx 0.09$ [4]. These numbers were used for the first iteration to evaluate critical parameters such as the tail arm, spans and areas. Further iterations were conducted to adjust for longitudinal & lateral stability, lighter weight and the minimum volume requirement for systems and setups. Corresponding to the shifting positions of the wing in weighing and balancing for stability, the volume coefficients were changed to $V_{HT} = 0.95$ & $V_{VT} = 0.09$ for constraining the CG variation inside the CG envelope. According to further evaluation of the stick-fixed neutral point versus horizontal tail volume coefficient, the value is well-fit to the general trend [4].

3.2 Aspect Ratio

The Aspect Ratios of tails were selected for the purpose of 1) a higher stall angle-of-attack than the wing, 2) a lower drag. As an $AR < 5$ would be performing with a high stall α [4], a higher AR in this range would reduce the induced drag, hence, based on these, the $AR_{HT} = 4$ and $AR_{VT} = 1.5$ were selected. Further investigation between the aspect ratio and the quarter sweep angle was conducted and turned out that these ARs are in the stable regime [9].

3.3 Tail Arm (l_{HT} & l_{VT}) & Tail Planform

Empirical equations and methods were applied for the initial sizing of the parameters of tailplanes [4]. A comparison between methods would be shown and a decision based on design requirements and mission profiles was made. According to the equation (18),

$$V_{HT} = \frac{l_{HT} \cdot S_{HT}}{c_{MGC} \cdot S_{Ref}} \quad V_{VT} = \frac{l_{VT} \cdot S_{VT}}{b \cdot S_{Ref}}, \quad (18)$$

the tail arm of both tailplanes could not be directly determined since the surface area of planforms is also an unknown variable. Hence, an alternative method involving the wetted area (S_{Wet}) is used. Due to the inverse ratio relationship between the tail arm and the tail area, it is assumed that the overall wetted area of the aft fuselage, horizontal & vertical tailplanes shall be constant. Referring to the equation (19), the wetted area would not change alone the variation of tail arms.

$$\frac{dS_{Wet}}{dl_T} = \frac{d}{dl_T} S_{Wet_{FUS}}(l_T) + \frac{d}{dl_T} S_{Wet_{HT}}(l_T) + \frac{d}{dl_T} S_{Wet_{VT}}(l_T) = 0 \quad (19)$$

In calculations of horizontal & vertical tail arms, comparisons were made between methods of considering either tail respectively and considering both tails together. In equation (20) - (22) the tail arms are calculated relative to the corresponding volume coefficient separately. The equations which consider

both horizontal and vertical effects are similar to these by combining the calculation of l_T with both V_{HT} & V_{VT} terms. Table (6) shows the results and differences between each other.

$$l_{HT} = \sqrt{\frac{V_{HT} \cdot S_{Ref} \cdot c_{MGC}}{D_{FUS}}} , \quad l_{VT} = \sqrt{\frac{V_{VT} \cdot S_{Ref} \cdot b_W}{D_{FUS}}} \quad (20)$$

$$S_{HT} = \frac{V_{HT} \cdot S_{Ref} \cdot c_{MGC}}{l_{HT}} , \quad S_{VT} = \frac{V_{VT} \cdot S_{Ref} \cdot b_W}{l_{HT}} \quad (21)$$

$$b_{HT} = \sqrt{AR_{HT} \times S_{HT}} , \quad b_{VT} = \sqrt{AR_{VT} \times S_{VT}} \quad (22)$$

b_W is the wing span and D_{FUS} is the diameter of the fuselage.

Assumptions were made initially, which state that the aft fuselage was shaped in a combination of a cylinder and a cone while the wetted area of the fuselage is approximated to the area of the side and top silhouettes [4]. The empennage length depends on the diameter of the fuselage. An initial guessed diameter was picked as $D_{FUS} = 3\text{ m}$. To maximise the tip-back angle, the lower limit of the ratio between the length of the empennage and D_{FUS} was chosen to be 3 [4]. Hence the length of the empennage, which is equivalently the height of the cone, $l_{emp} = 9\text{ m}$. By transforming the equations, the wetted area of the cone section turned out to be independent of l_T and only the cylindrical part needed to be considered.

Table 6: Comparison of results calculated by 2 methods

Parameters	HT	VT	Both	
			HT	VT
Tail Arm (m)	14.844	12.170		19.195
Area (m^2)	25.977	21.297	20.089	13.502
Span (m)	10.194	5.652	8.9641	4.500

One of the design requirements for the tail indicates that at most $1/3$ of the VT area could be blanked in the stalling stage. As a result, the first method which considered HT & VT respectively was chosen for a less shaded area from the horizontal tailplane since the tail arm for the horizontal is longer than that for the vertical one. This leads to that $l_{HT} > l_{VT}$ which mitigates the area being shaded.

Refer to past experimental and empirical data, to avoid the uncontrollable pitch-up of the horizontal tailplane at the stall, Figure [5] demonstrates the position of the tailplane in X and Z directions.

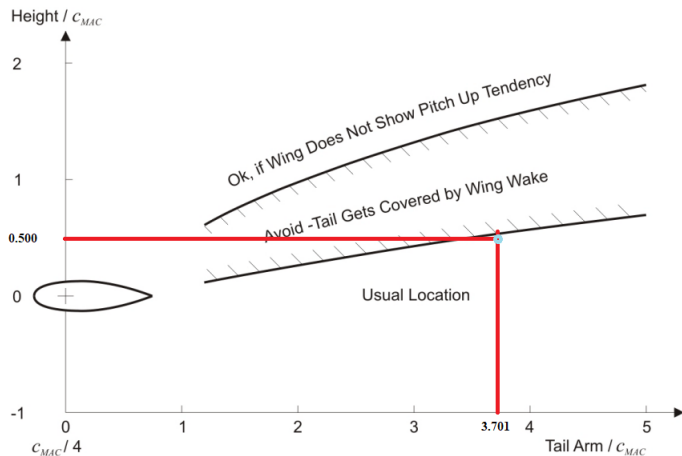


Figure 5: X and Z Position of the Tailplane aft Wing, background plot based on [1]

An initial value of $\frac{Z_H}{C_{MAC}} = 0.1$ was made. To fit the horizontal stabiliser to the empennage, a larger Z_H was needed. Therefore, by estimation and trial of fitting the wing and the horizontal tail in the side view, the $\frac{Z_H}{C_{MAC}} \approx 0.5$. With the l_{HT} calculated, the position of the tailplane relative to the wing is defined.

3.4 Sweep Angle (λ_{HT} & λ_{VT})

With a similar purpose as the wing, both horizontal tailplanes were designed with sweep angles for increasing the critical Mach number M_{crit} . To ensure that the horizontal plane could have the ability to level up the aircraft when in a diving situation, $M_{crit_{HT}} > M_{crit}$ is expected. With reference to equation (8), an iteration method was used to test the optimal quarter chord sweep angle $\Lambda_{c/4}$ (from 20° to 40°) under different drag divergence Mach number M_{DD} (from 0.7 to 0.8). In consideration of the $\Lambda_{c/4_{wing}}$, a larger sweep angle of 30.71° for the horizontal tailplane is used. Since the vertical tailplane would not be necessary for the diving-level-up situation, a smaller sweep angle of 27.61° was applied. For containing the design volume and area for the rudder, the trailing edge of the vertical tail was set to be almost vertical, hence, a larger $\Lambda_{c/4_{VT}} = 32.736^\circ$ was decided.

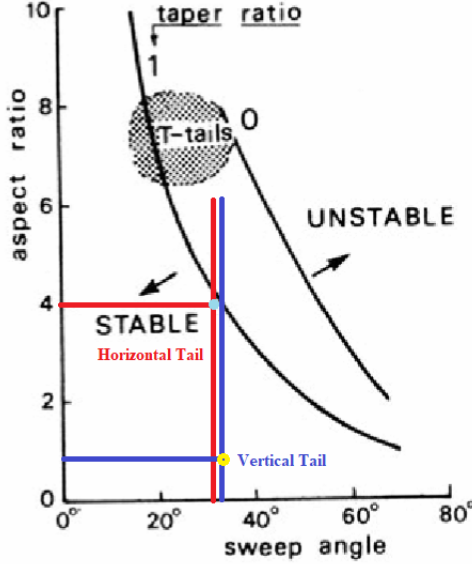


Figure 6: Design Point of Horizontal & Vertical Tailplane, based on the plot of [2]

Figure [6] shows the relationship between the aspect ratio and sweep angle for both tailplanes respectively with the horizontal in red and the vertical in blue. Notice that the lower black line has a taper ratio of 1 while the upper has 0. Since a λ_{HT} & λ_{VT} would be applied, the design points for the tailplanes are both in the stable area.

3.5 Taper Ratio (λ_{HT} & λ_{VT})

As the aforementioned design targets of the tails, the application of the taper ratio is essential in mitigating the induced drag to the tailplane, for reducing the effects of suction peaking at the tip and reducing the effect of tip separation caused by the sweep angle. Referring to [4], a $\lambda = 0.3$ provides the balance between the amount of induced drag and the feasibility of manufacture.

3.6 Aerofoil Selection

As the horizontal tailplanes mainly contribute to the longitudinal stability with varying lift force direction (+ve/ - ve), the aerofoil should have the range of lift coefficient approximately of $-0.3 < C_{l_{HT}} < +0.4$. In consideration of most of the lift is contributed from the wing, the $C_{l_{HT}}$ could be relatively smaller but $C_{d_{HT}}$ should be small. Also, one of the most important design considerations is the $\alpha_{stall_{HT}}$ should be higher than $\alpha_{stall_{wing}}$ as the tailplane could recover the nose pitch up after the main wing has stalled. Based on these, two types of aerofoils were considered, one is the NACA 63-212 while the other is the NACA 63-210. By analyses, NACA 63-210 has a closer value of C_l with $C_{l_{Design}}$ at its optimal α where gives highest L/D_{max} and the C_{M0} at α_{stall} is higher than that of NACA 63-212 [3]. Therefore the NACA 63-210 was chosen as the aerofoil of the horizontal tailplane.

In terms of the aerofoil of the vertical tailplane, the stall behaviour in the longitudinal direction is no longer significant. The main aim of the vertical tail is for lateral stability, such as the gust and OEI situations. Hence, a symmetric aerofoil is required and the NACA 0012 was selected for the $C_{l_{max}} = 1.3892$ at 15.5° and $\frac{t}{c} = 12\%$ [3]. These show that this aerofoil meets the design requirement for a high angle of attack and enough volume for containing all actuators.

3.7 Twist (ϵ_{HT}) & Dihedral (Λ_{HT})

Since the geometrical twist from the root to the tip is used for mitigating the tip separation brought by the sweep, in terms of the tailplane, the downwash generated from the wing would automatically reduce the effective angle of attack which generally produce similar effects with the twist. The boundary layer growth from the root to the tip would not be as significant as that of the wing. Therefore, the horizontal tailplane is designed with $\epsilon_{HT} = 0^\circ$.

Due to the reason that the tail was decided to be a conventional configuration, the longitudinal and lateral stabilities were responsible by horizontal and vertical stabilisers respectively. Therefore, the dihedral angle for the horizontal tailplane would not be important as most of the lateral disturbance would be recovered by the vertical tail. A $\Gamma_{HT} = 0^\circ$ was hence selected.

3.8 Summary of Tailplane Parameters

Table 7: Summary of Tailplane Parameters

Parameter	Horizontal	Vertical
AR	4.000	1.500
S_{ref} (m ²)	25.977	21.297
b (m)	10.194	5.652
λ	0.300	0.300
c_{root} (m)	3.921	5.797
c_{tip} (m)	1.176	1.739
$\Lambda_{c/4}$ (°)	30.710	32.736
Λ_{LE} (°)	36.077	37.865
Λ_{TE} (°)	10.766	3.407
Tail Arm (m)	14.844	12.170
M_{crit}	0.70	0.67

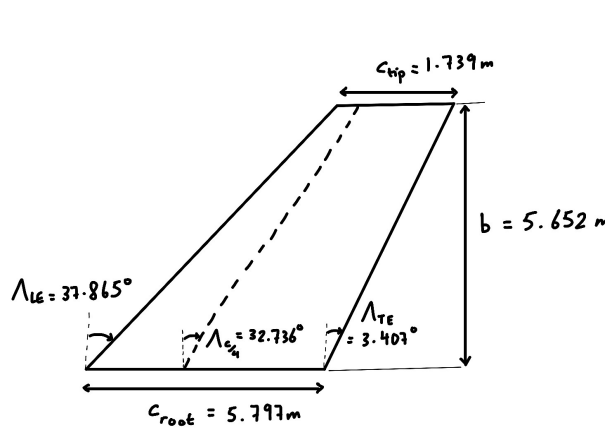


Figure 7: Vertical Tailplane Dimensions

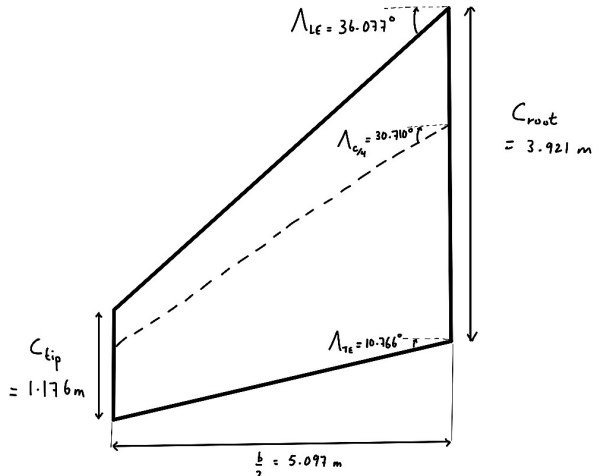


Figure 8: Horizontal Tailplane Dimensions

4 Control Surface Design

To obtain reasonable estimates for the sizing and location of control surfaces, data from similar regional jets is used at the conceptual design stage. Fully accurate sizing cannot be conducted without first performing a dynamic analysis of how the control surfaces responds to control inputs. This will be delved at a later stage of aircraft development.

4.1 Aileron Design

The aileron typically occupies 30% of the wing-span, as mentioned before. Thus an aileron span ratio, (b_a/b), of 0.30 is prescribed. Using historical data guidelines in Figure 9 [10], an aileron chord ratio, (c_a/c) of about 0.34 can be obtained as shown. However, since the flaps have chord dimension of $0.3c$, the same value of 0.30 is chosen for c_a/c such that the aileron is aligned with the flap.

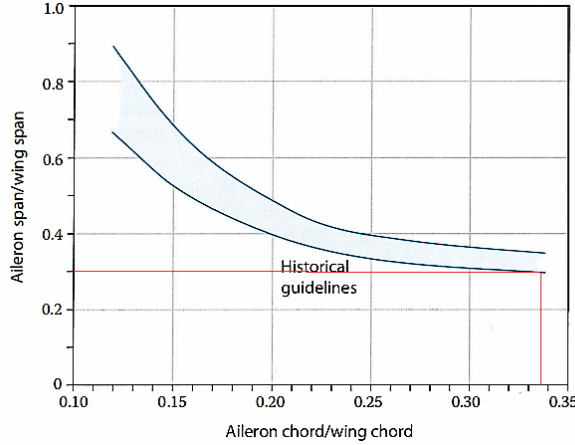


Figure 9: Historical Guidelines for aileron span and chord ratios

Ailerons are typically employed to provide better lateral control, specifically roll control, of the aircraft. This is determined by how much it changes the roll rate of the aircraft when deflected. Thus the maximum up and down deflection of the aileron is an important parameter to maximise effectiveness. Maximum aileron deflections ($\delta_{a_{max}}$) of $\pm 20^\circ$ are chosen based on the typical value for similar chord and span ratios of existing aircraft. A lower bound is chosen to minimise adverse yaw effects as well as flow separation effects at high angles of attack. Based on the same approach, a typical value of 0.07 is chosen for (S_a/S_{ref}). The inboard and outboard chord dimensions, c_i and c_o , are calculated using the same principles as wing chord calculation. Similarly, b_a for the wing semi-span is determined using the aileron span ratio. Lastly, to determine the location of the inboard(b_i) and outboard(b_o) portions of the aileron, considering that an initial 10% portion of the wing is left for fuselage placement, 58% is occupied by flaps, this allows for b_i and b_o to be placed at 68% and 98% of the semi-span. This means that the aileron outboard edge would be at 2% from the wing tip, making it prone to tip vortices, reducing the aileron efficiency. However, the inclusion of winglets would increase the tip efficiency to mitigate that effect. The aileron parameters are summarised in Table 8.

Table 8: Summary of aileron sizing parameters for wing semi-span

$\frac{b_a}{b}$	$\frac{c_a}{c}$	$b_i (\%) \frac{b}{2}$	$b_o (\%) \frac{b}{2}$	c_i (m)	c_o (m)	b_a (m)	S_a (m ²)	$\delta_{a_{max}} (\circ)$
0.30	0.30	68	98	1.33	0.33	4.27	3.54	± 20

4.2 Spoiler Design

Spoilers serve to increase the onset of drag at landing by causing the flow upstream of the wing to separate when deployed, thereby reducing the landing distance required by the aircraft. Figure 10 [5] illustrates this over a lifting surface. Spoilers are usually located forward of the flaps and aft of the maximum thickness point, typically occupying about 60% of the wing semi-span. The chord ratio is of the spoiler, (c_s/c) is usually based on the location of the front and aft spars and is usually within the

30 to 50% of wing chord range, whereby the C_D value is the highest. However, to accommodate wing components such as flaps, slats, ailerons, under-wing engines and other systems, c_s/c is chosen to be at a lower value of 0.25. The inboard position of the spoiler relative to the semi-span is selected to be identical to that of the flap (10% of $b/2$) for a more streamlined arrangement. A typical value of spoiler area ratio, $S_s/S_{ref} = 0.25$, is chosen.

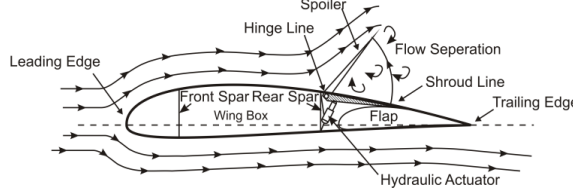


Figure 10: Operation of a spoiler

Based on the BOEING-737 data [6], a maximum spoiler deflection, $\delta_{s_{max}}$ of 60° is selected. Chord dimensions calculations are done following similar principles to that of the wing design. Table 9 showcases the selected and calculated parameters.

Table 9: Summary of spoiler sizing parameters for wing semi-span

$\frac{b_s}{b}$	$\frac{c_s}{c}$	$b_i (\%) \frac{b}{2}$	$b_o (\%) \frac{b}{2}$	c_i (m)	c_o (m)	b_s (m)	S_s (m^2)	$\delta_{s_{max}} (\circ)$
0.60	0.25	10	70	2.37	0.59	8.54	12.65	60

4.3 Rudder Design

The Rudder is an important component that makes up the vertical tail as it provides directional control of the aircraft. The design requirements are heavily dependent on the desired directional control and trimability conditions, in cases where sufficient yawing moment about the centre of gravity is required in order to counteract asymmetric thrust in a potential one-engine operative scenario for example. The rudder to vertical tail chord $\frac{c_r}{c_{vt}}$ was selected to be 0.4 which is typical for similar regional aircraft[4]. It is recommended also that the rudder starts on the fuselage and extends to 90 % of the semi-span of the tail, with a span ratio, $\frac{b_r}{b_{vt}}$ of 0.9. The reason for this value not being 1.0 is due to structural reasons. The surface Area of rudder to vertical tailplane ratio $\frac{S_r}{S_{vt}}$ is also found from empirical values and chosen to be 0.3[12]. The maximum deflection angle is one of the most important parameters and is calculated using the equation below.

$$\delta_r = \frac{T_L \cdot y_t}{-S_{ref} q \cdot b C_n, \delta_r} \quad C_n, \delta_r = -C_{L_{av}} \bar{V}_v \eta_v \tau_r \frac{b_r}{b_v} \quad (23)$$

Here, T_L is the force of thrust, y_t is the centre line distance of the aircraft to the engine, q is dynamic pressure which is taken at cruise speed, S_{ref} is the area of the wing, and b is the span. C_n, δ_r , is the directional control derivative. where $C_{L_{av}}$, \bar{V}_v , η_v and τ_r are the vertical tail's lift curve slope, vertical tailplane volume the tailplane efficiency factor and angle of attack effectiveness parameter [4]. The end value was found to be 30 degrees.

Table 10: Summary of rudder parameters

$\delta_r (\circ)$	$\frac{c_r}{c_v}$	$\frac{b_r}{b_v}$	$\frac{S_r}{S_v}$
30	0.25	0.9	0.3

4.4 Elevator Design

The elevator is also important as it is used to provide longitudinal control of the aircraft. Deflecting the elevator changes the lift at the horizontal tailplane and it does this by producing a pitching moment about the aircraft centre of gravity, which then alters the aircraft pitch. It is recommended also that the elevator starts on the fuselage and extends to 90 % of the semi-span of the tail giving a span ratio of $\frac{b_e}{b_H}$ of 0.9 with an elevator to horizontal stabilizer chord ratio, $\frac{c_e}{c_H}$ of 0.2511 for regional aircraft such as this

one. A value of 0.9 is chosen as it is within the range for an aircraft of this size[11] and for structural reasons. The surface area ratio of the elevator to the horizontal tail plane chord, $\frac{S_e}{S_H}$ is then chosen to be 0.20 [2]. The maximum deflection angle this time was found empirically[4] and a summary of the parameters are found below.

Table 11: Summary of elevator parameters

δ_e (°)	$\frac{c_e}{c_H}$	$\frac{b_e}{b_H}$	$\frac{S_e}{S_H}$
30	0.25	0.9	0.2

5 Fuselage Design

The fuselage design is comprised of designing three components: cockpit, cabin, and empennage. The maximum diameter of the fuselage (i.e. the diameter of the cabin) and the length of the cabin are determined directly through the target capability, constraints of human body spaces and standards of FAR25. Then, past data from similar regional jet aircraft are used as a reference to determine the range of lengths of the cockpit and empennage. Detailed sizing and internal layout for each component are subsequently found by fitting the necessities into the fuselage using CAD to produce 2D orthographic projections with making minor adjustments along the way to integrate the three components.

5.1 Cabin Design

The cabin is designed to accommodate 90 passengers and 5 crew members with their baggage with premium economy class standards and meet the FAR25 safety requirements. It is sufficient to have one passenger aisle for this narrow-body regional jet. FAR25 requires a maximum of three seats abreast for each side with one passenger aisle. Due to the compact nature of narrowbody aircraft, the seating in one row is chosen as a 2 - 3 arrangement.

The diameter of the cabin can be subsequently found as the summation of a width of 5 seats, aisle width (51 cm), gaps between passenger seats to the wall, and wall thickness on both sides. The seat width is chosen to be 56 cm to fit the first-class standard to ensure enough space for the possible modification to integrate the internal cabin layout. The typical wall thickness range for an aircraft is from 5 - 10 cm. The most efficient pressurised vessel, which features a sphere shape vessel, counteracts the out-of-plane stress as purely tensile stress. The net stress on the surface is given by

$$\sigma_{hoop} = \frac{PR}{t}.[4] \quad (24)$$

where P is the resultant pressure on the fuselage surface, which can be found through the pressure difference between the pressure in the cabin and the pressure in the flying condition. The pressure difference is taken as the worst-case scenario where the aircraft is flying at the highest altitude with the maximum pressure difference between the cabin and outside. R is the internal radius of the cabin without the wall thickness, and t represents the wall thickness. Looping through the thickness of the range 5 - 10 cm, the resultant strains of the surface associated with thickness are found to be in the same order of 10^{-5} . Hence, it is safe to choose 5 cm as the wall thickness. However, this approximation may not include all load cases in reality. Also, the wall thickness shall also consider the wall features, beams and skin. Hence, an increase of 5 cm to the thickness was applied.

The total length of the cabin is found through the number of rows for passengers, cross aisle and space for the crew, 2 lavatories, and emergency exit requirements. For this aircraft, one Type I, one Type III, and one Type IV emergency exit are required. For faster turn-around time, an extra type I emergency exit, instead of Type IV door, will be used at the rear, not only ensure the safety but also increase the efficiency of loading/unloading passengers. Figure [11] shows the top view of the fuselage layout.

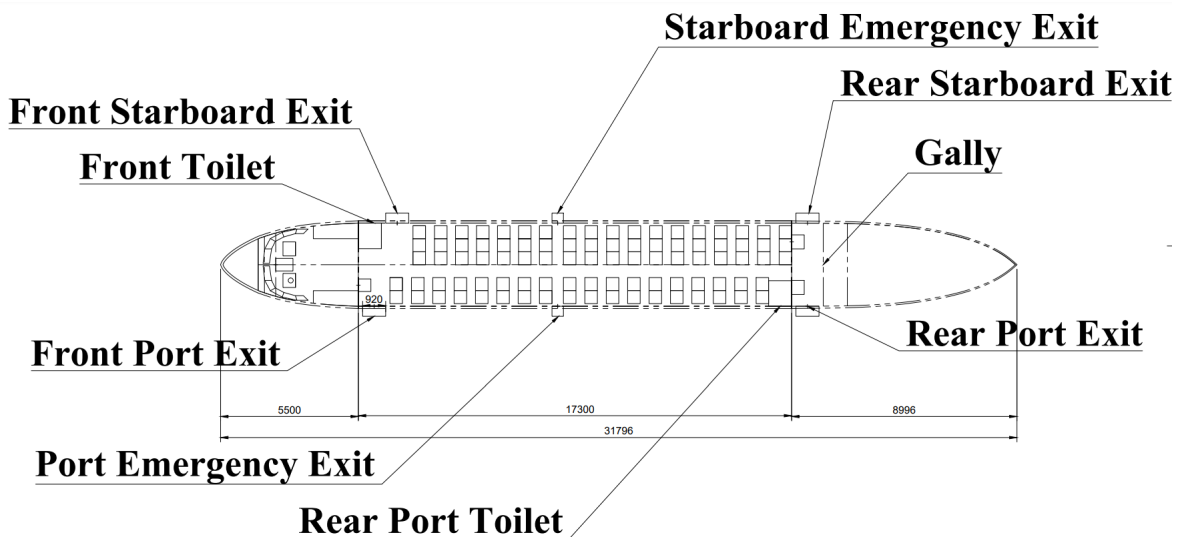


Figure 11: Top View of the Fuselage Layout

Assuming that in the worst-case scenario, each passenger carries 23 kg of check-in baggage. This requires approximately 15.8 m^3 space for storing in the underbelly cargo of the aircraft and 5.18 m^3 for the overhead bin storage. A safety margin of 15% was added since the volume would not be fully efficiently used during storage. The cross-sectional areas of the bin and underbelly storage are designed to ensure the total length is within a reasonable range. No ULD container was considered due to the limits of payload weight and the body scale of this design of the aircraft. With floor thickness to be approximately 0.05 times the fuselage diameter and a headspace greater than 1.93 m, the front view can be plotted, with seat width adjusting to 52 cm to satisfy all of the requirements. The windows are designed so that people within 5% to 95% can see outside at their eye level. 2 ladders are placed below the front and rear exits for purpose of quick turnaround time with less ground support equipment. Collecting information from the top and front views completes the side view and the cabin design. Figure [12] and [13] shows the Front and side view of the overall layouts.

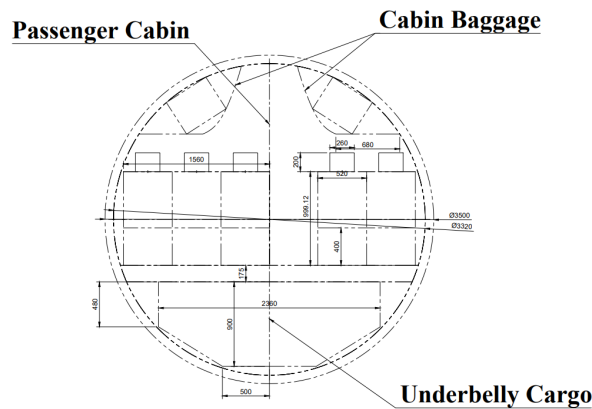


Figure 12: Front View of the Fuselage Layout

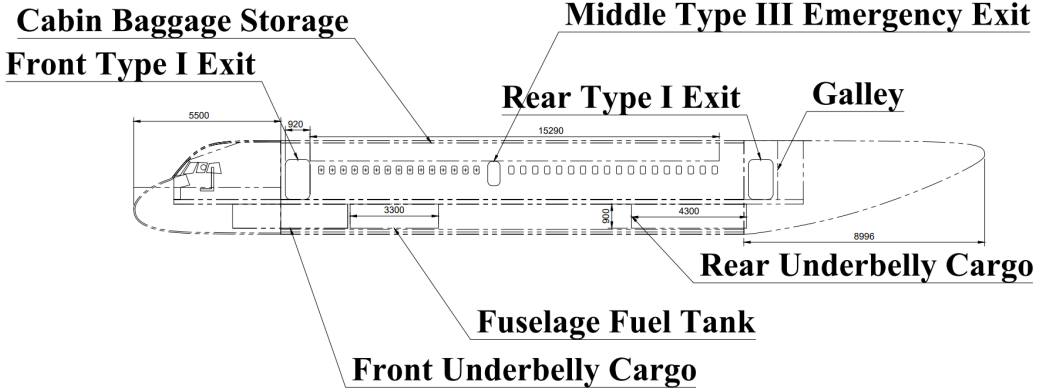


Figure 13: Side View of the Fuselage Layout

Total Fuselage Length (m)	31.796
Maximum Fuselage Diameter (m)	3.5
Fineness Ratio	9.08
Cockpit Length (m)	5.5
Empennage Length (m)	8.996
Upsweep Angle ($^{\circ}$)	12
Cabin Height (m)	2.110
Floor Thickness (m)	0.173
Pitch Distance (m)	0.852

Table 12: Design Parameters of the Fuselage

5.2 Empennage Design

In cabin design, aerodynamic performances are generally not the primary concern, as the perimeter and length of the cabin are dominated primarily by structural and commercial requirements. Hence, to optimise the aerodynamic performance, more can be done on optimising the length and overall shape of the empennage.

Skin friction drag varies directly with the wetted area. Minimum friction drag is therefore achieved through the minimum fuselage wetted area. The empennage fineness ratio with the least skin-friction drag is found to be around 2.58[4]. However, for typical regional jet transport aircrafts, the aft fineness ratio ranges from 2.6 to 4 [10], with increasing skin-friction drag as the fineness ratio increases. Having designed the cabin, the most constraining remaining parts to fit into the empennage are the galley and the Type I emergency door. These can all be fit into the empennage with the smallest fineness ratio in the range. Therefore, the aft fineness ratio is chosen to be 2.6, with a total length of 8.996 m.

Blunt empennage should be avoided as it promotes adverse pressure gradient, which leads to flow separation and causes higher profile and base drag. An upsweep angle greater than the angle of attack of C_{Lmax} at lift-off is introduced to ensure that the aft body does not touch the ground during takeoff. From past data, it is reasonable to have an upsweep angle within the range of 15 - 19 $^{\circ}$, as a higher upsweep angle introduces more drag. For this aircraft, the upsweep angle is chosen to be 12 $^{\circ}$ rather qualitatively as the optimal angle can only be found through further aerodynamic analysis with CFD. Sharp corners are designed to reduce drag and alleviate lateral oscillation caused by vortex-induced flow separation at the upsweep surface.

5.3 Cockpit Design

The cockpit length can be found in two approaches, either directly through the typical range of fineness ratio of the cockpit, or by finding the range of the total length of the aircraft and subtracting the lengths of cabin and empennage derived from the previous two parts. To ensure the cockpit length satisfies both

criteria and is more generic, the cockpit length is chosen as 5.5 m, which falls within the intersectional results from both approaches above.

The typical body-related geometrics with its statistical variations, including arm, leg, window-eye distance and seat-eye distance, are taken into account to ensure that pilots can control the aircraft easily.

Good visibility means that the pilot should be able to see the immediate surrounding and be alert of the traffic outside the window. Windows should also be designed to achieve smaller profile and base drags, as the bluntness causes flow separation. Figure [14] & [15] show the top and side view of the cockpit, with labels of body clearance with the cockpit equipment such as the overhead panel. These also prove that the visibility and the windows' geometric designs fit the requirement.

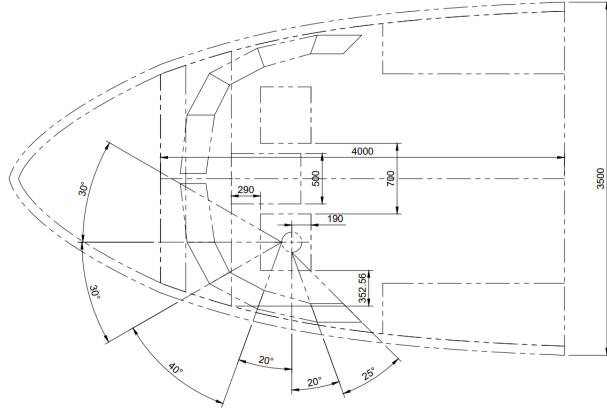


Figure 14: Top view of cockpit

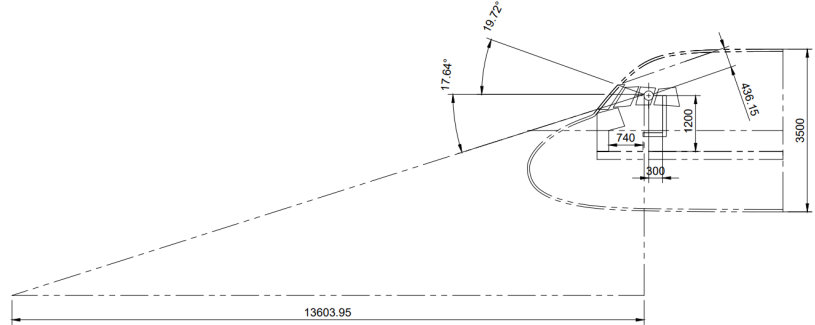


Figure 15: Side View and Minimum Viewing Distance from the Cockpit

The final length chosen for the cockpit is 5.5m to accommodate all the constraints, systems, nose gears and other avionic equipment.

6 Propulsion System Design

6.1 Propulsion Selection

Cruise speed, altitude and range are some aircraft metrics that are dependent on the thrust produced by the engine. In addition to meeting the required thrust the aircraft demands, it must satisfy regulations as well as be easy to maintain and reliable in order to reduce the turndown time as much as possible. From historical flight envelope data [11] turboprop and turbofan engines were both viable engines. A turbofan was chosen over a turboprop. Although the turboprop did outperform the turbofan in terms of fuel efficiency at the speed and altitude the aircraft will be cruising, this came at the cost of increased noise coming from the large propellers. Given the low wing configuration and the appeal of turbofan to airliners as well as passengers, a turbofan was chosen with a podded under-wing placement for ease maintains

but at the cost of increased chances of bird strikes. More specifically, a high bypass ratio turbofan was chosen for better efficiency. A propfan or 'Open rotor Engine' was also considered since theoretically it can provide the speed and performance of a turbofan, with the fuel economy of a turboprop [12]. However, this type of propulsion is very much still in its development phase and faced challenges when brought to the market shown by the General Electric GE36 being discontinued after 4 years after its first run in 1989 [13] with only proposals to implement it onto aircrafts. The very low ground clearance of a propfan as well as the increased noise coming from multiple small fans also compounded its drawbacks. From Figure[2], the $(T/W)_0 = 0.2886$ gave a total required installed thrust of 130kN so 65kN per engine. The engines would be in a podded underwing configuration so incoming airflow would not be affected by the fuselage and the exhaust gas would not affect the tailplane.

6.2 Engine Installation

All the engines shortlisted in table 13 were tested uninstalled so the testing did not account for losses in the form of intake pressure and bleed air losses. The thrust loss due to non-ideal pressure recovery was calculated to be 2.7% per engine using Equation (25).

$$T_{loss} = C_{ram} \left(\left(\frac{P_1}{P_0} \right)_{ref} - \left(\frac{P_1}{P_0} \right)_{actual} \right) \quad (25)$$

with the inlet ram recovery correction factor $C_{ram} = 1.35$ for subsonic flight [[10]] and assuming ideal pressure recovery ($(P_1/P_0)_{ref} = 1$) and $(P_1/P_0)_{actual} = 0.98$ for real subsonic podded inlet. The aircraft must also provide power to power the cabin pressurisation, climate control, as well as de-icing systems, therefore there will be bleed air losses. Using (26)

$$T_{LossBleed} = C_{Bleed} \frac{\dot{m}_{Bleed}}{\dot{m}_{engine}} \quad (26)$$

and approximating $C_{Bleed} = 2$ [[14]], the mass rate of bleed to be 3% and 12% for the engine mass flow due to the use of bleed air for the pneumatic and electrical systems gave a thrust loss due to bleed of 5% per engine. Therefore the total thrust lost during installation sums to 8.7% per engine, so the chosen engine must provide a minimum of 70.3 kN of thrust.

6.3 Engine Selection

Table 13 are some turbofan that has/had been in production. The scale factor was applied to the length, height and weight to adjust the thrust accordingly using Equation(10.1-10.3)[10]. Specific fuel consumption (SFC) was considered but not compared directly since some manufacturers would publish the SFC at sea level but it was more common to see the SFC of engines during cruise at different altitudes, speeds and temperatures.

Table 13: Shortlisted Engine with Length, Height and Weight Adjusted

Engines	T_0 (kN)	SF	Length(m)	Height(m)	Weight(kg)	Bypass Ratio
GE CF34-8C5 [[15]]	64.5	1.09	3.37	1.41	1220	5.0:1
R-R Tay 650-15 [[16]]	67.2	1.05	2.45	1.17	1600	3.1:1
R-R BR710 C4-11 [[17]]	68.4	1.03	4.71	1.81	1880	3.8:1
P&W PW815GA [[18]]	71.2	0.988	3.30	1.25	1400	5.5:1
PowerJet SaM146 [[19]]	71.6	0.983	3.57	1.21	2220	4.4:1

It was clear that the best choice out of the shortlist was the Pratt & Whitney PW815GA; not only did it provide the highest bypass ratio and second lightest dry weight out of the five engines but the uninstalled thrust was only $\approx 1.12\%$ higher than the required thrust, so rubberising the engine would be unnecessarily costly and time-consuming. On the downside, there was no published data on either the sea level or cruise SFC values from P&W or by Gulfstream Aerospace, the only company that uses the engine for their Gulfstream 600 business jet. So a cruising SFC of 0.535hr^{-1} was estimated using equation 27 which included a 20% improvement in SFC due to generational improvement [10]. Although the SFC value for the P&W engine was significantly lower than the two closest comparable engines: the

PowerJet SaM146 and the Rolls Royce BR710 C4-11 having SFC_{cruise} values of 0.629hr^{-1} and 0.656hr^{-1} respectively [19] [17], the company has shown it was capable of producing efficient engine like with the P&W PW1400G used for the Irkut MC-21 having an SFC_{cruise} value of 0.513hr^{-1} [20].

$$SFC_{cruise} = 0.8 * 0.88e^{-0.05BPR} \quad (1/\text{hr}) \quad (27)$$

6.4 Capture Area and Inlet Sizing

A pitot style inlet was selected as the inlet for its theoretical 100% pressure recovery at subsonic speed, in reality, the value will be lower due to viscosity and further investigation will require detailed nacelle geometry and CFD analysis. The nacelle placement and its geometry need to provide minimal distortion as well as negate rotating stalls and any surges. From historical data [10] aligning the nacelle 2° nose down and 2° inward cant ensure no distortion with local flow under the wing. For the majority of the time, the aircraft will be in cruise when it is in use, so the inner lip radius will be 8% of the inlet radius and 4% for the outer radius to reduce drag, minimise distortions with the added benefit of the reducing the effect of AoA during takeoff and landing [10]. In order for the engine to operate efficiently, the incoming air must be slowed down twice, from cruising at $M=0.69$ to $M=0.54$ at the front of the inlet then a further reduction to $M=0.39$ at the front of the engine itself.

The capture area must be optimal to ensure no air spillage in front of the engine increasing drag or hindering the required air intake for the engine thus decreasing thrust. Based on isentropic flow relation, equation (28) & [29], $A_{Throat}/A_{Engine} = 0.7825$ and with a fan diameter of 1.225 m (non-rubberised) plus 10% to factor in the nacelle inner diameter, housing the ventilation system and gearbox, resulted in an analytical capture area of 1.116m^2 . The length of the nacelle was estimated to be 5.393 m using equation (30) where $k = 1.6$ for a regional transport jet [21].

$$\frac{A}{A^*} = \frac{1}{M} \left(\frac{1 + 0.2M^2}{1.3} \right)^3 \quad (28)$$

$$\frac{A_{Throat}}{A_{Engine}} = \frac{(A/A^*)_{Throat}}{(A/A^*)_{Engine}} \quad (29)$$

$$L_{Nacelle} = L_{Engine} + kD_{Engine} \quad (30)$$

6.5 Nozzle Geometry

For cost and ease of maintenance, a fixed nozzle design was chosen over a variable-area nozzle which provides better performance but in the supersonic regime. A nozzle area was estimated to be 0.6 times the capture area and the nozzle length to be 0.75 times the fan-face diameter [10].

6.6 Engine Integration

The turbofan will be situated at 30% of the semi-wing span [21]. Requirements were it must be high enough not to decrease the landing and takeoff AoA. Clearance greater than 15cm beyond a 5° roll on the undercarriage was the optimum height for the engine. Pylons will be used to attach the engine to the LE spar, with easy access to the fuel, electrical and pneumatic systems for maintenance.

Table 14: Engine Property & Nacelle Geometry

Capture Area (m^2)	1.116
Inlet Radius (cm)	60.00
Innerlip Radius (cm)	4.800
Outerlip Radius (cm)	2.400
Nozzle Area (m^2)	0.6696
Nacelle Length(m)	5.393
Engine Weight(kg)	1422

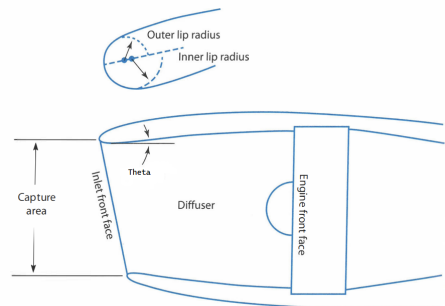


Figure 16: Layout of Pitot Inlet

7 Structural Layout

7.1 Fuselage Structure

The fuselage will consist of longerons running the whole length of the fuselage with frames/braces spaced appropriately to minimise obstruction with doors and windows and to maintain the fuselage shape. A central wing box running through the fuselage was selected. One of the advantages of a low-wing configuration was that there was less dependency on heavy supports at the wing root. A thicker longeron running along the bottom of the fuselage may be required to attach the nose landing gear and thicker braces may be placed around where the main landing gears.

7.2 Wing and Tailplane Structure

Twin-spar was selected for the wing to allow space for fuel tanks in between the spars with ribs to maintain the aerodynamic shape. Thicker and heavier ribs will be placed where the engine and undercarriage will be mounted as well as the connection point of the wing and fuselage. LE and TE spar will be placed at 10% and 75% of the local chord to allow extra space for the fuel and hydraulics. The LE spar will provide a convenient point to add the hinge system for the slats; likewise for the TE spar for the elevators, spoilers and ailerons. For the empennages, the vertical and horizontal stabiliser both will have a twin-spar design located at 15% and 65% a convenient hinge point for the trim devices.

7.3 Dynamic Loading Considerations

Instigation into the effects of dynamic loading cannot be fully explored in the conceptual phase, also there are some design considerations that could counteract some dynamic wing behaviours. For example, the twin-spar design also provides more resistance to torsion in conjugation with the upper and lower wing skin creating a 'box' beam design, this will help to reduce any dynamic aeroelastic behaviour like flutter. Placing the engine on the TE not only aid with the aircraft's CG placement but it placement keeps the engine's CG forward of the TE hinge line, reducing the chance of aileron reversal from control surface flutter. The separation of the wing fuel tank in conjunction with the ribs will prevent excess sloshing, reducing CG lateral movement.

7.4 Material Selection

Aerospace grade aluminium would be used the most for most of the aircraft, due to its balance property of tensile strength, weight and relative cost to manufacture compared to more exotic material. Due to its cost and difficulty in manufacturing, titanium alloys are used sparingly, mostly for engine components like the compressor fore half-section and the fans to keep the cost down making the aircraft more appealing for airliners while the rest will be made out of nickel-based alloy. Although the cost and manufacturing methods have improved dramatically for composites, predicting and detecting failure has not been researched enough to warrant its implementation into structurally critical components like longerons or ribs. On the other hand, for weight-saving benefits, using composites for landing gear doors, tailplanes and fuselage and wing skins could be considered.

8 Aircraft Systems Layout

Due to the design requirement for 30 minute turnaround time as well as ease of maintainability and reliability, an emphasis on decentralised systems, ease of part replacement and future-proofing was important in choosing the system layout.

8.1 Fuel System

The mass of the fuel required from initial design was 13.3×10^3 kg, taking the density of Jet A-1 fuel as 805 kg/m³. To account for the different values for the fuel [22] as well as to comply with FAR §25.969, an extra 4% increase in volume was added summing to 17.0 m³. However, since L/D for cruising fell below the expected value of 17.2, the aircraft's range and endurance were short of the mission profile. Given the empty weight was also below our design W_e shown in Table[16], extra fuel weight was added and a revised weight of 13.8×10^3 kg. Consequently, the revised fuel volume was 17.6 m³. Extra volume of 0.621 m³ able to store 500 kg of reserve fuel was added for extreme cases like extra cargo or a small

fuel leak occurring during cruise.

The majority of the fuel will be stored inside the wing, using integral tanks. The tanks will be situated in between the LE and TE spar and 30% and 85% of the chord measuring from root to tip as shown in Figure[17] to ensure no interference with engine and main landing gear placement. The fuel in the wing will be split into 3 tanks situated between structural ribs to reduce sloshing during banked turns. The surge tanks are placed up to 90% of the semi-span to reduce the probability of critical lightning strikes. Each tank will have two fuel pumps for redundancy and the surge tanks will be fitted with overflow return valves satisfying regulations. Therefore a 20% reduction in volume was implemented to account for the structural integrity, the unused volume due to the integral tanks as well as the space taken for the fuel pumps and the hydraulic systems.

Taking the reduction into account, approximating the fuel volume in the wing using the trapezium rule resulted in a volume of 11.0 m^3 , the rest of the fuel will be placed in a central tank, placed in the fuselage with a volume of 6.70 m^3 with the reserve fuel volume accounted for. The fuel tanks in the wing will be filled first and fuel usage will start at the tip moving to the wing root; when the engine requires fuel from the closest wing tank, the central fuel tank will keep this tank full if required.

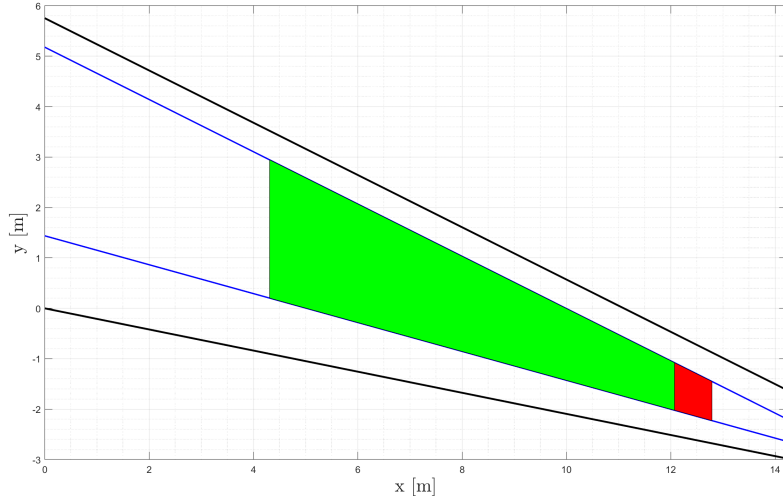


Figure 17: Wing Fuel System. Red area indicates the surge tank.

Table 15: Fuel Distribution across the aircraft. [†] Surge tank not accounted for in volume/weight summary

Location	Volume (m^3)	Weight (kg)
Wing Tank x2	11.0	8.86×10^3
Centre Tank	6.70	5.39×10^3
Surge [†] x2	0.475	383
Total	17.7	1.43×10^4

8.2 Hydraulics and Pneumatic

A 2H/2E system was selected for its proven reliability in the A380 [23] with 4 independent power sources (2 electrical and 2 hydraulics systems). Each engine has an electrical generator and hydraulic pump. Critical lifting surfaces (i.e. ailerons, elevator and rudder) as well as flaps and slats use a conventional hydraulic system with an Electrohydrostatic Actuator (EHA) used as redundancy. Although the conventional hydraulics system makes replacing the system harder than an EHA, its proven reliability was far more critical than the extra cost and time spent on inspections and replacement. Bleed air from the engine will be used to pressurise the cabin and aid in climate control as it will be less taxing on the electrical system.

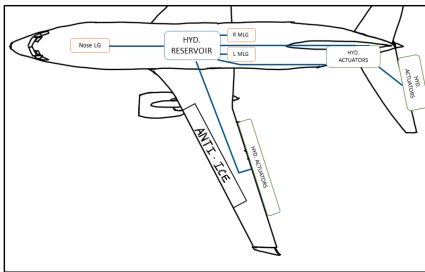


Figure 18: Basic Hydraulic System (drawing not indicative of final design)

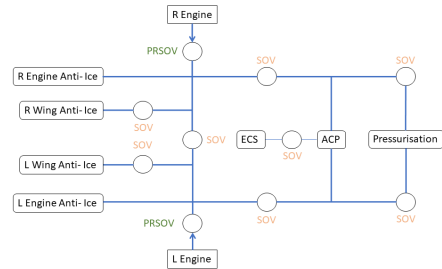


Figure 19: Basic Pneumatic Diagram

8.3 Electrical System

The fast turnaround time means that reliance on a ground power unit (GPU) was not possible. Therefore a jet-fuel auxiliary power unit (APU) using the fuel from the centre tank, situated at the tail, would be used instead to provide power for lighting and climate controls when on the ground.

The electrical system powers a large amount of equipment (i.e. avionics, climate control, food preparation, infotainment, flight controls etc [24]). The primary source of power will be coming from the electric generators from each engine, any excess will be stored in 24V batteries placed around the aircraft; 2 near the avionics system and 2 near the tail to keep CG centre. The secondary power source will come from the batteries, the APU as well as the ram air turbine placed near the tail.

Figure [20] shows the basic electrical system. The electric generator from the engine produces AC and travels to relevant components via the AC bus, the Transformer Rectifier (TR) converts AC to DC and the essential DC bus allows the DC to go where it is required the most like avionics. A portion of the direct current from the TR passes through the DC battery bus where it is stored in the batteries. On the other side of the plane, an extra pair of batteries are placed on the other side if Battery 1 & 2 are at full capacity. The electric engine starter motor uses power from Battery 3& 4 to start both engines. In the scenario where there is no power stored in the batteries, the APU could be utilised to start the engines.

If the primary system fails, the APU and batteries are deployed automatically, supplying power to the AC and DC essential bus respectively like communications and the digital flight recorder log. A portion of AC generated by the APU can be converted to DC if the batteries are drained. Non-essentials like lighting and infotainment will be turned off. The RAM will be deployed near the tail if the APU is unable to supply enough AC to the systems. Wiring should be routed through different parts of the aircraft to evenly distribute the weight along the centerline of the aircraft and can be easily accessed with cables being able to carry more than the rated 60kV in case of electrical surges.

8.4 De-Icing System

Temperature can hit freezing temperatures in all three airports, so a reliable de-icing solution was important during consideration. Slats disable the use of pneumatic deicing boots, the dependence on deicing fluids with a limited capacity would increase the turnaround time, and the extra electrical power consumption required eliminated the use of electro-thermal heating elements since the system is not reliant on Ground Power Units (GPU). As a result, bleed air in conjunction with an icephobic coating was chosen. In sub-zero conditions, the left engine running idle could be instead on an APU to provide power to the cabin as well as bleed air when grounded. This would eliminate any dependency on external aid to prevent ice formation. The loss of performance, during climb or cruise in freezing conditions, due to bleed air was considered not much of a concern since the engines provide more thrust than required and the APU could be used to aid in cabin lighting and pressurisation.

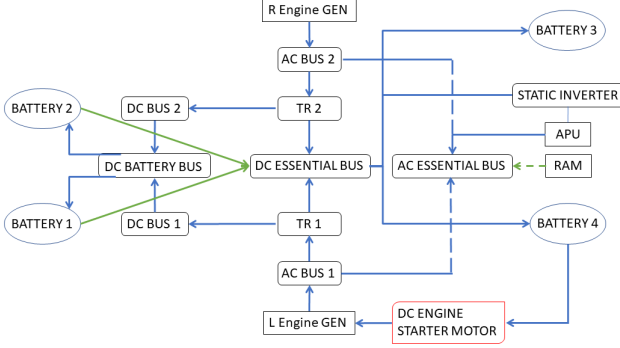


Figure 20: Basic Diagram of the Electrical Systems. Lines in **green** are Used During Primary System Failure.

8.5 Avionics

Listed below are some components that are installed into the aircraft and placed near the cockpit to reduce wiring. Systems that are bold-highlighted are considered critical and should have 3 redundancy in place, the rest should have one backup. To reduce pilot training time, the cockpit should have a familiar layout similar to comparable aircraft like the Embraer E-jets with modern features like heads-up displays and modular digital display interfaces.

- **Navigational Aid**
- **Communication & EICAS**
- Flight Management and Auto pilot
- Information Displays
- **Digital Flight Records**
- **Fault Detection & Maintenance Alert System**

9 Weight and Balance

9.1 Weight Estimation

The maximum takeoff weight (MTOW) deduced in the initial sizing only made use of empirical relations without breaking down the weight into separate components forming part of the aircraft. At this stage, sizing the major components of the aircraft can only be done through estimations and comparisons of existing data for similar aircrafts. Using empirical methods and equations from [25], the weights of the most important components can be estimated in imperial units. To simplify the balance calculations, the placement of the components can be done simultaneously with the sizing. A breakdown of the obtained results is presented in Table 16. The weight of the handling gear is accounted for in the MTOW summation but not displayed in the table as its weight is so low that it does not impact the balance.

Summing up the component weights and adding the payload and fuel weights yields a takeoff weight of 96545 lbs, which is 43792 kg when expressed in SI units. This falls short of the estimated MTOW by only 4.57%, indicating a very reasonable estimation. This allows the airline operator the flexibility of carrying more fuel as a contingency measure in case of leakages or to increase the range of the aircraft and accommodate extra or overweight luggage.

9.2 Balance Estimation

To estimate the centres of gravity in the x and z directions, an arbitrary reference point of $(x,z) = (0,0)$ was set at the nose tip of the aircraft for the datum. Based on this, the x and z positions of the components were estimated based on existing aircraft such as the AIRBUS A220 [A220]. Estimates from

Table 16: Breakdown of Weight and Balance estimations. \dagger y_{CG} for furnishing was estimated to be 2.8 ft

Component	Weight	x position	z position
Wing	7334.5	39.22341	-4.6088
Horizontal Tailplane	898.93	87.924	1.9703
Vertical Tailplane	764.2	79.14992	103.05
Fuselage	11349	45.89974	0.0000
Main Lan	3523.1	43.92717	-1.3000
Nose Landing Hear	666.62	5.93914	-1.4000
Nacelle	1700.8	32.14598	-6.6667
Engine	6269.9	32.14598	-6.6667
Engine Control	61.434	16.07299	-3.4566
Engine S	132.80	32.14598	-6.6667
Fuel System	471.50	35.30107	-4.6088
Flight Control	1104.8	51.39856	10.831
APU	330.00	99.10171	2.2966
Instruments	240.15	9.84252	0.0000
Hydraulic System	189.34	39.22341	-2.8707
Electrical System	719.46	35.30107	-2.8707
Avionics	2141.4	3.740157	-2.8707
Furnishing \dagger	5399.5	41.72703	3.2808
Air-Conditioning	1129.3	52.15879	4.5932
De-Icing System	202.33	26.06724	-4.6088
Passengers	15906	36.71979	0.8538
Baggage	4563.6	41.72703	-2.2966
Fuel	31416	39.11909	-4.6088
Total Weight	96545		
CG Position		39.54	-2.003

[25] are also employed. The positions of the overall aircraft x_{CG} and z_{CG} are estimated using

$$(x_{CG}, z_{CG}) = \left(\frac{\sum W_i x_{CG}}{\sum W_i}, \frac{\sum W_i z_{CG}}{\sum W_i} \right) \quad (31)$$

which takes into account the x_{CG} and z_{CG} positions of each component (i^{th} component) as well as their respective weights.

The CG positions are estimated for every necessary loading case of the aircraft in order to size the undercarriage and calculate the stability for the worst case scenario. These are defined to be:

1. Empty weight
2. Pilots and minimum fuel to fly last leg cruise
3. Pilots and minimum fuel to fly 3 legs
4. Crew, Passengers, Payload and minimum fuel for mission

The CG values obtained for each of these cases can be summarised in Table 17. A noteworthy assumption made about the CG positions was the fact that the overall CG would not change by a significant amount as fuel is consumed since most of the fuel is stored in the wings.

Table 17: CG locations based on loading cases

Load Case	Mass (lbs)	x_{CG} (ft)	z_{CG} (ft)
1	44659	40.34	-1.16
2	57978	40.05	-1.92
3	76406	39.83	-2.57
4	96545	39.54	-2.00

From these, the following CG envelope can be plotted to visualise the range of CG required for safe flight requirements.

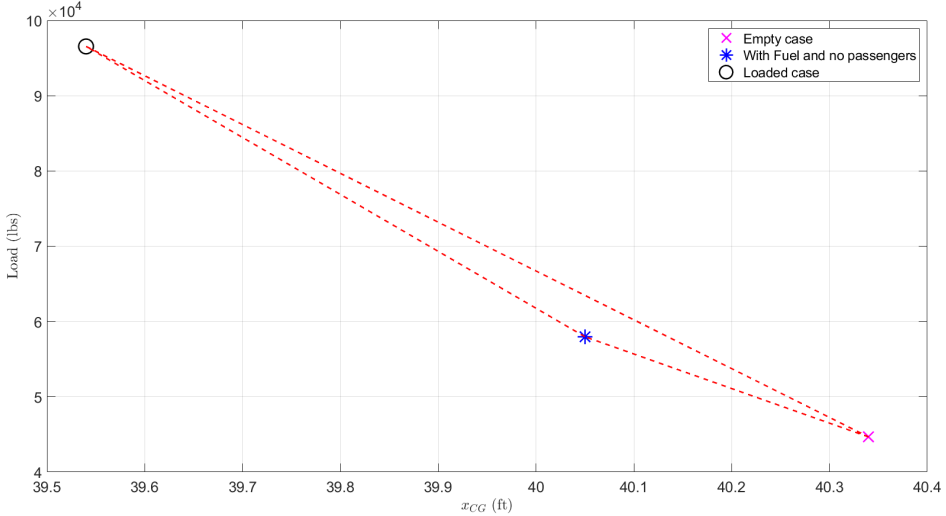


Figure 21: CG envelope for specified load cases

10 Undercarriage Design

10.1 Layout

A tricycle configuration was chosen for the undercarriage for its inherent stability on the ground. As W_0 is greater than 50,000 lbs but less than 200,000 lbs there are 2 wheels per main undercarriage and nose strut. The two main struts are placed on the wing at 15% of the wing semi-span (to ensure that the engine and main gear are sufficiently far apart) and will fold inwards towards the fuselage, while the nose will fold forwards due to fuselage space constraints.

10.2 Positioning

The initial undercarriage positioning was calculated based off the centre of gravity without the undercarriage included. Initially, the main struts were to be placed on the trailing edge spar at 75% of the local chord of the wing, but due to the position of the aft and foremost centre of gravity this position was too far backwards and thus the nose gear would have too much load applied on it. It was therefore decided that the main gear would be placed on an additional horizontal spar at 50% of the root chord of the wing. For sufficient clearance between the main gear wheels and engine the main gear was placed at 15% of the wing span. Equations (32) and (33) detailed below are used.

$$W_0 - W_{ng} - W_{mg} = 0 \quad (32)$$

$$W_0 x_{CG} - W_{ng} x_{ng} - W_{mg} x_{mg} = 0 \quad (33)$$

Following an initial choice of x_{CG} and x_{mg} values, x_{ng} was decided such that at the aftmost CG would have 8% of the total aircraft load; however, due to storage constraints in the fuselage this was then revised and the nose gear was moved further aft. This resulted in 9.1% and 12.6% of the load on the nose gear for aft and foremost CGs respectively. These values are within the range of 5% to 20% recommended[26]. From these positions, the CG was updated to include undercarriage and the overturn and vertical CG angles were calculated. These angles were then recalculated once the tyres were chosen to account for tyre shape change under loading. Table 18 shows these values.

Table 18: Table comparing overturn angle, vertical centre of gravity angle and load on nose gear for the aftmost and foremost centre of gravity positions

Parameter	Aftmost	Foremost
Overtake ($^{\circ}$)	35.7	36.7
Vertical CG ($^{\circ}$)	17.0	22.9
PAX load on gear (%)	9.1	12.6

These satisfy the condition that overturn angle should be less than 63° and the vertical CG angle greater than the tipback angle[27], calculated to be 10.5° . For these calculations, the convention shown in Figure 22 was used, where $z = 0$ was the middle of the maximum diameter of the fuselage (the nose tip).

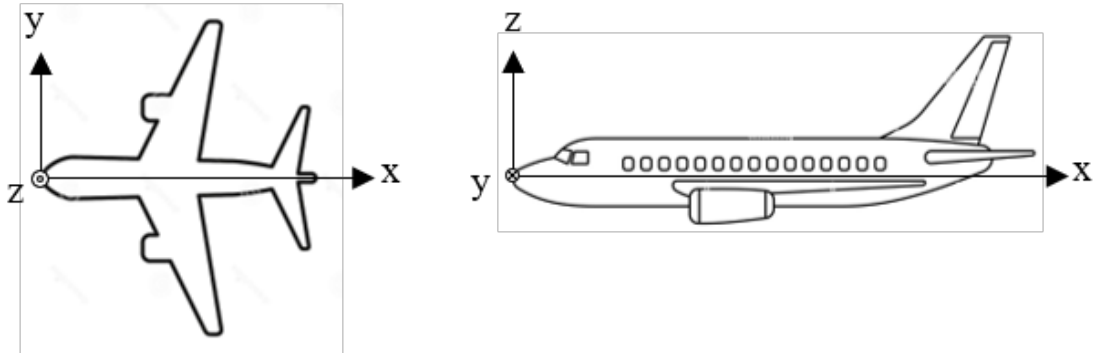


Figure 22: Diagram showing the origin defined for overturn, vertical CG angle and clearance calculations

The graphs plotted for these calculations for aftmost and foremost CG are displayed and the final position of the gears are summarised in Table 19 below.

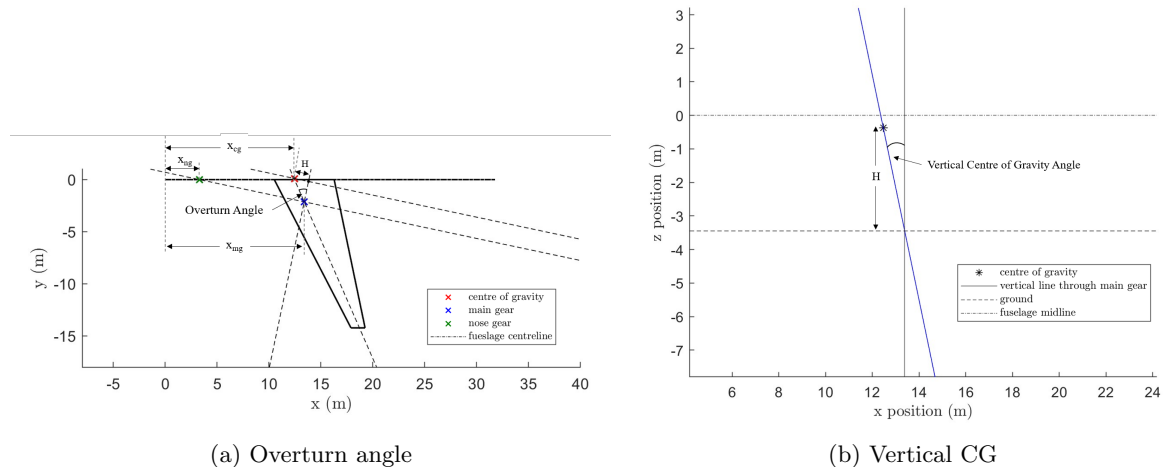


Figure 23: Graph showing the lines drawn to calculate the overturn angle and vertical CG angle for the aftmost CG case. This was repeated for the foremost CG

Table 19: Table summarising the final x-position of the main gear, nose gear and centre of gravity

x_{mg} (m)	x_{ng} (m)	$x_{CG_{aft}}$ (m)	$x_{CG_{for}}$ (m)
13.39	3.30	12.47	12.12

The lengths of the main gear struts were determined to provide suitable clearance for the engines, as shown below.

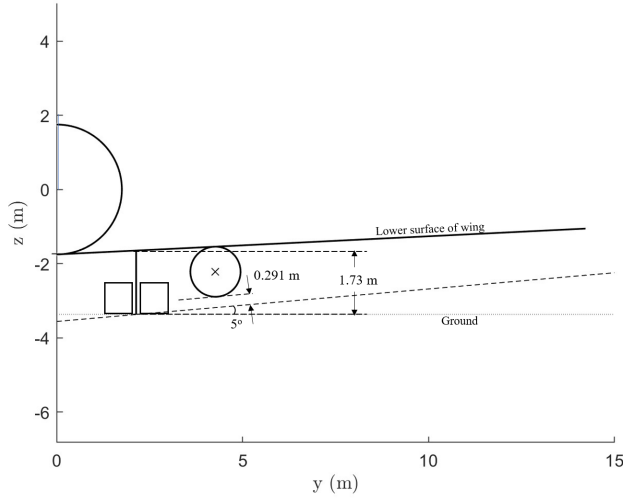


Figure 24: Graph showing how the engine clearance was determined

The engine clearance is calculated to be 0.291 m above the 5° line, which is greater than the required clearance of 0.152 m (6 inches). The nose gear length was then decided based off the main gear, as it was preferable to have the fuselage floor level. To prevent wheel shimmy, the nose gear was given a positive rake of 7°.

10.3 Tyre Choice and Sizing

The tyres were chosen based off the static and dynamic loads that each wheel would experience which were calculated using

$$W_w = \frac{\text{Static Load on strut} \times 1.07}{\text{Number of wheels on strut}} \quad (34)$$

$$W_{dn_{u/c}} = \frac{10 H W_0}{g B} \quad (35)$$

where H is the aircraft centre of gravity height above the static ground line (ft), B is the distance between x_{mg} and x_{ng} and this is for an assumed 10 ft/s² deceleration. From this the following loads were calculated as shown in Table 20 and consequently the tyre selection was made using tyre data from GoodYear Aviation Databook [28].

Table 20: Table displaying the calculated loads per wheel and subsequent tyre choices. RL = Rated Load, RBL = Rated Braking Load, P = Pressure, R = Radius, A = Area

Wheel	W_w (lbs)	Size	RL (lbs)	RBL (lbs)	P (PSI)	Roll R(in)	Contact A (in ²)
Nose	6.81×10^3	22x8.50-11	10000	15000	210	4.32	32.42
Main	2.41×10^4	37x14.00-14	25000	37500	160	15.44	153.77

All runways had a tyre pressure limit of 254 psi and were flexible. The pressure of the chosen tyres is suitably lower than this value. The ACN values were then calculated for these pressures and loads using COMFAA[29], and the results are shown below.

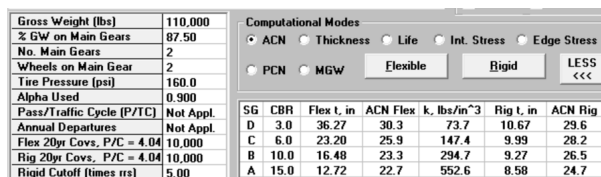


Figure 25: Calculation of ACN values using COMFAA

The ACN values are visibly lower than the PCN values for each of the runways – 64, 60 and 45 for Wellington, Christchurch and Hamilton respectively – and thus these wheels are suitable choices.

10.4 Shock Absorber Design

An oleo-pneumatic telescopic shock strut was chosen for the shock absorber. The calculated dimensions are summarised in Table 21 and were calculated using the following equations to determine the stroke and external diameter of the oleo respectively.

$$S = \frac{V_v^2}{2g\eta N_g} - \frac{\eta_T}{\eta} S_T (+1 \text{ inch}) \quad (36)$$

$$D_{oleo} \approx 0.04\sqrt{L_{oleo}} \quad (37)$$

where N_g is the gear load factor (typically $\approx 2.7 - 3.0$), η is the shock absorber efficiency, η_T is the tyre efficiency, V_v is the touch-down sink speed

Table 21: Nose and Main gear specifications. L = Length, δ = deflection

Gear Type	Stroke L (in)	Oleo δ (in)	Oleo L (in)	Oleo ext.diameter (in)
Nose Gear	10.0	6.67	25.0	5.72
Main Gear	10.0	6.67	25.0	5.78

The stroke length was calculated individually for the nose and main gears via conservation of energy, giving values of 2.49" and 3.83"; however it is recommended that a minimum of 10" [30] is used and thus this value was chosen for both as a safety factor.

11 Aerodynamics - Drag Estimations

The total drag of the aircraft is calculated for each segment of the mission, including 3 takeoffs, 3 cruises, and 3 landings. For each segment, the parasite drag and lift-induced drag are calculated and added together to give the total drag.

First, A rough estimation of the parasite drag is obtained from the Rapid Drag Estimation Model[15] as a reference. Then, the Component Drag Buildup Method[10] is applied to account for contributions from the wing, horizontal tailplane, vertical tailplane, fuselage, and nacelle. Miscellaneous drags from flaps, fuselage upsweep, and undercarriage are added per the configuration in the specific segment. Wave drag is also considered during the cruise. The leakage and protuberance effects are considered in every configuration. A summary of the drag results for each section is provided.

11.1 Parasite Drag (Zero-Lift Drag)

11.1.1 Rapid Drag Estimation Method

A low-fidelity but fast method to estimate the parasite drag as a reference is the Rapid Drag Estimation Method[15] based on the presumed relationship between the aircraft wetted area and its averaged skin friction, and C_{D0} . Compared to the Equivalent Skin-Friction method proposed by Raymer, which can only approximate the parasite drag coefficient in cruise, this method involves the drag components of high-lift devices in ΔC_{D0} , providing a more comprehensive estimation:

$$C_{D0} = (f/S + \Delta C_{D0})k_{crud} \quad (38)$$

Where f is the equivalent flat plate area, an idealised value that can be found from interpolating the graph of Roskam[14], Perkins, and Hage[31]. $C_{D0} = 0.0218$ is found using this method.

11.1.2 Component Buildup Method

As written in equation (39), the Component Buildup Method considers the different types of drag from each component, hence proving high-fidelity results. The term S_{wet}/S_{ref} is used to scale the sizing of the aircraft component so that their drag can be added in the same scale. The following table summarises what aircraft components needs to be considered in different segment of the mission.

	Wing	HT	VT	Fuselage	Nacelle	Flaps	Undercarriage	Fuselage Upsweep
Takeoff	×	×	×	×	×	×	×	×
Cruise	×	×	×	×	×			×
Landing	×	×	×	×	×	×	×	×

Table 22: Drag from aircraft components in different mission stages

$$(C_{D0})_{subsonic} = \frac{\sum C_f FF Q S_{wet}}{S_{ref}} + C_{D,misc} + C_{D,L\&P} \quad (39)$$

However, during the cruise, as the Mach number is relatively larger, the compressibility effect should also be taken into account since shock appears in some parts of the aircraft where the local Mach number is greater than 1, causing an additional pressure drag. Hence equation (39) is slightly modified to obtain equation (40).

$$(C_{D0})_{cruise} = \frac{\sum C_f FF Q S_{wet}}{S_{ref}} + C_{D,misc} + C_{D,L\&P} + C_{Dw} \quad (40)$$

The remaining of this subsection presents the detailed calculations of different drag components.

Skin-Friction Drag Coefficient C_f

The skin-friction drag results from viscosity, leading to the formation of boundary layers. At higher Reynolds numbers, the friction drag is much higher as a result of turbulence than that of lower Reynolds numbers in the laminar regime. Equations (41) and (42) present the averaged skin friction drag coefficient from the leading edge to the trailing edge for laminar and turbulent conditions, respectively. The total friction drag for each aircraft component can be calculated by a weighted sum. The turbulence boundary layer is assumed to be 90% for the wing, horizontal and vertical tailplanes, 95% for the fuselage and nacelle.

In the laminar regime, skin friction can be directly obtained from equation (41)[32], for which the local Reynolds number is calculated with the characteristic length of the aircraft component: total length for the fuselage and the mid-chord length for the wing and tail sections.

$$C_{f,laminar} = \frac{1.328}{\sqrt{Re}} \quad (41)$$

In the turbulent regime, Prandtl-Schlichting relation[33] is applied. The effective Reynolds number should be used for this model. Effective Reynolds number is obtained through the minimum value of the cutoff Reynolds number Re_{cutoff} and the local Reynolds number. Surface roughness k is assumed to be 2.08×10^{-5} ft for this aircraft with smooth paint.

$$C_{f,turbulent} = \frac{0.455}{(\log_{10} Re)^2 \cdot 58(1 + 0.144M^2)^{0.65}} \quad (42)$$

$$Re_{cutoff} = 38.21(l/k)^{1.053} \quad (43)$$

Form Drag Factor FF

The form drag evaluates the pressure drag of the component. For wing and tail sections with $t/c \leq 0.21$, Torenbeek's method[2] can be applied, as presented in equation (44), where the sweep Λ_m and x/c are taken as the sweep of maximum-thickness line and chordwise location of maximum thickness, which is typically 0.5 for high speed aerfoils [10].

$$FF = \left[1 + \frac{0.6}{(x/c)_m} \left(\frac{t}{c} \right) + 100 \left(\frac{t}{c} \right)^4 \right] [1.34 M^{0.18} (\cos \Lambda_m)^{0.28}] \quad (44)$$

Skin Friction	Wing	HT	VT	Fuselage	Nacelle	Total C_f
Takeoff 1	0.00250	0.00265	0.00250	0.00193	0.00250	0.01208
Takeoff 2	0.00239	0.00253	0.00239	0.00185	0.00239	0.01155
Takeoff 3	0.00245	0.00260	0.00245	0.00190	0.00246	0.01186
Cruise 1	0.00220	0.00234	0.00220	0.00172	0.00221	0.01067
Cruise 2	0.00223	0.00254	0.00239	0.00185	0.00239	0.01140
Cruise 3	0.00222	0.00235	0.00222	0.00173	0.00223	0.01075
Landing 1	0.00255	0.00272	0.00255	0.00197	0.00256	0.01235
Landing 2	0.00243	0.00258	0.00243	0.00188	0.00244	0.01177
Landing 3	0.00253	0.00269	0.00253	0.00195	0.00253	0.01222

Table 23: Summary of skin-friction coefficient C_f

According to Raymer[10] and Nicolai[34], the form drag factor for a smooth fuselage can be found through

$$FF = 1 + \frac{60}{f^3} + \frac{f}{400}, \quad (45)$$

where $f = 9.08$ is the fineness ratio of the fuselage.

The form drag factor for the nacelle is calculated as

$$FF = 1 + \frac{0.35}{f}[10] \quad (46)$$

Form Drag FF	Wing	HT	VT	Fuselage	Nacelle
Takeoff 1	1.1395	1.0890	1.1371	1.1027	1.0389
Takeoff 2	1.1966	1.1436	1.1942	1.1027	1.0389
Takeoff 3	1.1626	1.1111	1.1602	1.1027	1.0389
Cruise 1	1.4384	1.3747	1.4355	1.1027	1.0389
Cruise 2	1.4213	1.3583	1.4184	1.1027	1.0389
Cruise 3	1.4297	1.3664	1.4268	1.1027	1.0389
Landing 1	1.1116	1.0624	1.1094	1.1027	1.0389
Landing 2	1.1727	1.1208	1.1703	1.1027	1.0389
Landing 3	1.1243	1.0745	1.1220	1.1027	1.0389

Interference Factor Q

The typical interference factor Q can be found in Raymer, listed as the table below

	Wing	HT	VT	Fuselage	Nacelle
Q	1	1.05	1.05	1	1.5

Table 24: Drag from aircraft components in different mission stages

Miscellaneous Drag Coefficient $C_{D,misc}$

During takeoff and landing, the undercarriage, flaps, and slats are deployed, resulting in larger parasite drags. The drag of the u/c is calculated as

$$C_{Du/c} = 2.25 \frac{A_{u/c,front}}{S_{ref}} \quad (47)$$

Since slats do not contribute to drag, only drag due to flaps is considered. The takeoff flap angle is considered as 15° , and the landing flap angle is taken as 40° , which are the typical reference values from similar aircraft, B737.

$$C_{D,HLD} = 0.0023 \left(\frac{b_f}{b} \right) \delta_f \quad (48)$$

The drag contribution from fuselage upsweep should be considered in every configuration. The upsweep angle β is designed as 12° .

$$C_{D,upsweep} = 3.83 \left(\frac{\pi d^2}{4S_{ref}} \right) \beta^{2.5} \quad (49)$$

	Takeoff Flaps	Fuselage Upsweep	U/C	Landing Flaps
Misc Drag	0.00020	0.00731	0.04302	0.00052

Table 25: Summary of Miscellaneous Drag Coefficient $C_{D,misc}$

Leakage and Protuberance Drag Coefficient $C_{D,L\&P}$

A safety factor of 5% will be added to the total parasite drag to account for the leakage and protuberance drag.

Wave Drag Coefficient C_{Dw}

The wave drag is calculated using Lock's empirical model[35] by fitting the experimental data on the transonic drag rise. The critical Mach number M_{crit} is found to be 0.5161 through the rearranged and simplified Korn's Equation[35] as follows.

$$M_{critical} = (\kappa - 0.108) - (t/c) - 0.1C_l \quad (50)$$

$$C_{Dw} = 20(M - M_{critical})^4 \left(\frac{S_{exp}}{S_{ref}} \right) \quad (51)$$

Wave Drag	C_{Dw}
Cruise 1	0.01605
Cruise 2	0.00491
Cruise 3	0.00910

Table 26: Summary of Wave Drag Coefficient in Cruise

11.2 Total Drag Coefficient

11.3 Total Trimmed Drag

In the cruise stage, the total drag is found to be the sum of the parasite drag and the lift-induced drag:

$$C_D = C_{D0} + K[C_{L\alpha}(\alpha + i_w - \alpha_{ow})]^2 + \eta_h \left(\frac{S_h}{S_{ref}} \right) K_h C_{Lh}^2 \quad (52)$$

In the above equation, K is the drag-due-to-lift factor, and there are two ways of estimating it as presented below sections: 1. Through the classical wing theory (Oswald Span Efficiency Method) with Oswald efficiency factor e to account for the non-elliptical distribution nature of lift. This method is an underestimate of drag, as it is very idealised; 2. Through the Leading Edge Suction Method, which takes into account the lift curve slope for different cruises, and hence this is a more accurate method.

Oswald Span Efficiency Method

$$K = \frac{1}{\pi A e} \quad (53)$$

Leading Edge Suction Method

$$K = \frac{\alpha C_L}{C_L^2} = \frac{\alpha}{C_L} = \frac{1}{C_{L\alpha}} \quad (54)$$

Trimmed Drag	C_D LE	C_D Oswald
Cruise 1	0.04357	0.04063
Cruise 2	0.03222	0.02933
Cruise 3	0.03641	0.03350

Table 27: Summary of Trimmed Drag

Total Drag in Takeoff and Landing During takeoff and landing stages, lift-induced drag components from the extension of the flaps contribute to the total drag. And hence Δ_{Di} should be added to the parasite drag to find the total drag.

$$\Delta C_{Di} = k_f^2 \Delta C_L^2 \cos \Lambda_{c/4} \quad (55)$$

Takeoff/ Landing Drag	C_D
Takeoff 1	0.08744
Takeoff 2	0.08707
Takeoff 3	0.08729
Landing 1	0.08797
Landing 2	0.08757
Landing 3	0.08789

Table 28: Summary of Total Drag C_D during Takeoff and Landing

12 Stability and Trim

12.1 Stability

12.1.1 Longitudinal Static Stability

The aircraft's longitudinal static stability needs to be met to ensure that airspeed remains stable [5]. The neutral point of the aircraft, x_{np} – defined as the point of action of the lift on the whole aircraft – is coupled with downwash derivative ($d\epsilon/d\alpha$), tailplane efficiency factor (η_h), lift-curve slopes of the wing and tail ($C_{L_\alpha W}$ and $C_{L_\alpha h}$), fuselage pitching moment derivative ($C_{M_{\alpha f}}$) and tailplane-to-wing area ratio (S_h/S_W).

Fuselage Pitching Moment Derivative ($C_{M_{\alpha f}}$)

The fuselage pitching moment coefficient is evaluated using the following empirical relationship, defined about the centre of gravity:

$$C_{M_{\alpha f}} = K_f \frac{L_f w_f^2}{\bar{c} S_W} \quad (56)$$

, where L_f is the fuselage length, w_f the fuselage maximum width (i.e the diameter) and K_f , the fuselage and engine nacelle moment factor, a function of the quarter-chord position, evaluated as 1.25 rad^{-1} for a quarter-chord position of about 45% of fuselage length as shown on the graph below [36]. This yields a value of $C_{M_{\alpha f}} = 1.199 \text{ rad}^{-1}$.

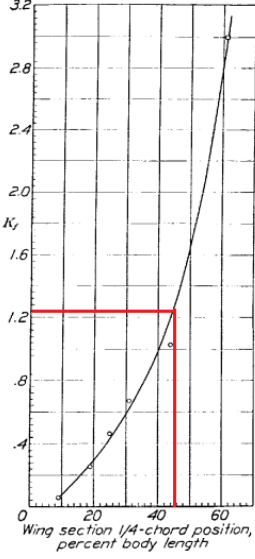


Figure 26: Variation of K_f with relative location of wing and body

Downwash Derivative ($d\epsilon/d\alpha$)

The downwash derivative is a function of wing aspect ratio, taper ratio, tailplane position, wingspan and wing lift-curve slope. It can be calculated using the following empirical relation [37]:

$$\frac{d\epsilon}{d\alpha} = 4.44 \left[K_A K_\lambda K_h \sqrt{\cos(\Lambda_c/4)} \right]^{1.19} \frac{C_{L_\alpha W} @ M_{op}}{C_{L_\alpha W} @ M = 0} \quad (57)$$

, where M_{op} is the Mach number at which the aircraft operates and K_A , K_λ and K_h are empirical functions of wing aspect ratio, wing taper ratio and horizontal tailplane position respectively. These can be evaluated using the following equations [37]:

$$K_A = \frac{1}{AR} - \frac{1}{1 + AR^{1.7}} \quad (58)$$

$$K_\lambda = \frac{10 - 3\lambda}{7} \quad (59)$$

$$K_h = \frac{1 - |h_h/b|}{\sqrt[3]{2l_h/b}} \quad (60)$$

, where l_h is the horizontal separation between wing and tailplane CGs and h_h is the vertical separation between wing root and horizontal tailplane. Evaluating the downwash equation at different operational Mach Number yielded a value of 0.356 for takeoffs and landings and a maximum value of 0.338 at cruise.

Neutral Point and Stability Evaluation

Using the aforementioned values, the neutral point can be evaluated for the the takeoff, landing and cruise at different mission segments where the tail and wing lift-curve slopes are calculated. The x_{np} is determined using the following empirical relation [37]:

$$\frac{x_{np}}{\bar{c}} = \frac{C_{L_\alpha W} \frac{x_{acw}}{\bar{c}} - C_{M_\alpha f} + \eta_h C_{L_\alpha h} \left(1 - \frac{d\epsilon}{d\alpha}\right) \frac{S_h}{S_W} \frac{x_{ach}}{\bar{c}}}{C_{L_\alpha W} + \eta_h C_{L_\alpha h} \left(1 - \frac{d\epsilon}{d\alpha}\right) \frac{S_h}{S_W}} \quad (61)$$

, where η_h is assumed to be 0.9 for a conventional tail clear of wing aft wake, x_{acw} and x_{ach} are the aerodynamic centres of the wing and tailplane respectively. The x_{acw} is assumed to be at the quarter-chord of the wing throughout flight since the aircraft operates at low transonic speeds [38].

The pitching moment derivative empirical equation is coupled with the power-off static margin, K_n , as follows:

$$\frac{dC_M}{d\alpha} = - \frac{dC_L}{d\alpha} \left(\frac{x_{np} - x_{CG}}{\bar{c}} \right) = - \frac{dC_L}{d\alpha} K_n \quad (62)$$

This implies that K_n must be positive to satisfy longitudinal static stability. This value is calculated in the power-off configuration. When the engines are on, thrust effects must be accounted for as engines would provide a negative pitching moment. Static margin will therefore be increased by an estimated 2 %. Thus, an empirical relation is used based on historical data for transport jets [10] to account for this increase and evaluate the static margin in power-on configuration as follows:

$$K_{n_{power-on}} = K_{n_{power-off}} - 0.02 \quad (63)$$

The K_n for takeoff, landing and cruise at the specified mission segments were calculated for the worst case scenario whereby the aircraft has minimum fuel requirement, no onboard passengers, two pilots and is in power-on configuration. The results, showcased in Table 29, depict that the aircraft will be longitudinally stable, meeting the requirements of a typical static margin in the range of 5% to 20% when compared to similar regional jets. Since the K_n is reasonable for the worst-case scenario, the aircraft is expected to be longitudinally stable when fully loaded.

Table 29: Summary of K_n analysis in power-on configuration

Mission Flight Segment	x_{CG} (ft)	x_{np} (ft)	K_n (%)
Wellington Takeoff	40.03	41.59	11.45
Wellington Cruise	40.03	41.75	12.59
Wellington Landing	40.03	41.58	11.43
Christchurch Takeoff	40.03	41.60	11.53
Christchurch Cruise	40.03	41.73	12.48
Christchurch Landing	40.03	41.59	11.50
Hamilton Takeoff	40.03	41.59	11.48
Hamilton Cruise	40.03	41.74	12.54
Hamilton Landing	40.03	41.58	11.44

A slightly larger K_n value is notable for cruise segments due to the reduced manoeuvrability of the aircraft during this flight phase, requiring more static margin to maintain longitudinal stability. The slightly lower K_n value at landing implies that the pilot can have better manoeuvrability of the aircraft for landing segments as there would be less fuel onboard. The x_{CG} value was assumed to have negligible change following fuel consumption as explained in weight and balance.

12.1.2 Directional stability

Due to the asymmetry of the seating arrangement creating a constant y_{CG} , lateral directional stability of the aircraft in flight must be considered. Directional static stability of an aircraft is determined by the yawing moment due to sideslip derivative. It quantifies the tendency of the aeroplane to turn into wind in the presence of a sideslip disturbance and engage into a roll [39]. When the slip angle changes, static lateral stability of the aircraft must be considered. While aerodynamic models exist for such an analysis, they were determined to be too complex for this conceptual overview and it was decided that the aileron would serve to provide lateral and directional stability by having a constant deflection as control input throughout flight.

12.1.3 Trim analysis

Trim flight implies that the sum of pitching moments about the x_{CG} is zero and the sum of the lift forces is equal to the aircraft weight. These conditions can be summarised empirically as follows [37]:

$$C_L = \frac{W}{\frac{1}{2}\rho V^2 S_W} \quad (64)$$

$$C_{M_{CG}} = -C_{LW} \left(\frac{x_{acW} - x_{CG}}{\bar{c}} \right) + C_{M_oW} + C_{M_{of}} \alpha - \eta_h C_{Lh} \frac{S_h}{S_W} \left(\frac{x_{ach} - x_{CG}}{\bar{c}} \right) + \frac{Z_t T}{q S_W \bar{c}} = 0 \quad (65)$$

, where C_{LW} and C_{Lh} are the lift coefficients of the wing and horizontal tailplane respectively, Z_t is the vertical moment arm of the thrust line from z_{CG} , taken to be 1.823 m, T is the effective thrust, C_{M_oW}

is the wing zero-lift pitching moment coefficient and q is the dynamic pressure. Thrust in flight can be assumed to be equal to the drag to balance forces during cruise. This leads to

$$T = D = qS_W C_D \quad (66)$$

which can be replaced back into equation 65. C_D is found from the aerodynamics analysis. C_{M_oW} can be evaluated empirically using

$$C_{M_oW} = \left[C_{M_{\alpha_f}} \left(\frac{AR \cos^2(\Lambda_{c/4})}{AR + 2 \cos(\Lambda_{c/4})} \right) - 0.01\epsilon \right] \frac{C_{L_{\alpha}W} @ M_{op}}{C_{L_{\alpha}W} @ M = 0} \quad (67)$$

, which is evaluated to be -0.0231. C_{L_W} and C_{L_h} are also coupled with the the cruise lift coefficient, $C_{L_{cruise}} = 0.3937$. This can be expressed in terms of the aircraft weight as follows:

$$C_L = C_{L_W} + \eta_h \frac{S_h}{S_W} C_{L_h} = \frac{W}{qS_W} \quad (68)$$

To solve for C_{L_W} and C_{L_h} , an iterative approach was adopted for the simultaneous solving of equations (65) and (68). The only extra unknown was α , defined to be the trim angle (α_{trim}) of the aircraft. A range of α_{trim} from -5° to 25° with a 0.01° increment was defined. α_{trim} can be further correlated to the C_{L_W} , zero-lift incidence of the wing (α_{0W}), wing setting angle (i_w) and $C_{L_{\alpha}W}$ as follows:

$$\alpha_{trim} = \frac{C_{L_W}}{C_{L_{\alpha}W}} - i_w + \alpha_{0W} \quad (69)$$

The C_{L_h} value can be empirically related to i_w , the tail setting angle (i_h), $d\epsilon/d\alpha$, α_{trim} , α_{0W} , the tailplane zero-lift incidence (α_{0h}), tailplane lift-curve slope ($C_{L_{\alpha}h}$), elevator deflection (δ_E) and elevator lift-curve slope ($C_{L_{\delta_E}}$). Rearranging the equation in terms of tail setting angle gives

$$i_h = \frac{C_{L_h} - C_{L_{\delta_E}} \delta_E}{C_{L_{\alpha}h}} - (\alpha_{trim} + i_w - \alpha_{0W}) \left(1 - \frac{d\epsilon}{d\alpha} \right) + (\alpha_{0h} - \alpha_{0W}) + i_w \quad (70)$$

A range from -3° and 15° with an increment of 1° was set for i_h within the iterative code, matching typical values [37]. Based on an initial guess of α_{trim} , equations (65), (68), (69) and (70) are iterated through a for loop until convergence. These yield optimal values for C_{L_W} and C_{L_h} which further yield optimal results of α_{trim} , i_w and i_h . These are summarised in Table 30 below:

Table 30: Summary of K_n analysis in power-on configuration

Mission Flight Segment	C_{L_W}	C_{L_h}	α_{trim} ($^\circ$)	i_w ($^\circ$)	i_h ($^\circ$)
Wellington Cruise	0.323	0.0372	1.41	0.50	-2.00
Christchurch Cruise	0.471	-0.0247	-1.18	1.50	-3.00
Hamilton Cruise	0.392	-0.0030	0.00	0.50	-1.00

α_{trim} is zero at $i_w = 0.5^\circ$ and $i_h = -1^\circ$. These parameters are thus chosen as the design points to maintain level fuselage at cruise. The normalised $C_{M_{CG}}$ is plotted against normalised C_L for the iterative trim analysis based on the specified ranges for the angles, as illustrated below.

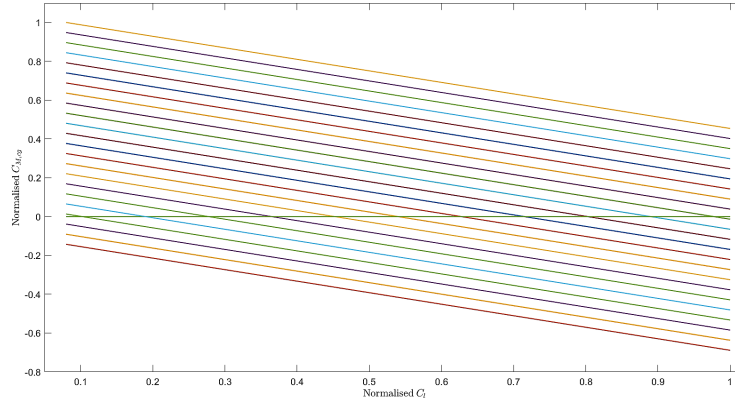


Figure 27: Iterative $C_{M_{CG}}$ vs C_L for different values of α_{trim} , i_h and i_w

13 Aircraft Performance

13.1 Take-off distance

The total takeoff distance of an aircraft consists of four key distances which are the ground roll, rotation, transition and climb distance, which have to be calculated. Additionally to this, a 15 % safety factor must be applied for the total takeoff distance which is a requirement with the FAR 25 regulations[37]. The equation then becomes as follows.

$$S_{TO} = 1.15(S_g + S_r + S_{tr} + S_{cl}) \quad (71)$$

In order to calculate the ground roll distance S_g , which is the distance travelled by the aircraft from a stationary position, V_1 on the runway till just before it begins to rotate V_{LOF} , equation(72) was used, where $K_A = \frac{\rho}{2(W/S)} \left(\mu C_L - C_{D0} - \frac{C_L^2}{\pi A Re} \right)$ and $K_T = \frac{T}{W} - \mu$, where μ is the rolling resistance of 0.05[15] for wet conditions. Wet conditions are used instead of dry as it is more constraining out of the two, and will ultimately produce the maximum takeoff distance.

$$S_g = \frac{1}{2gK_A} \ln \left(\frac{K_T + K_A V_{LOF}^2}{K_T + K_A V_1^2} \right) \quad (72)$$

To calculate the rotation distance, S_r which is the distance the aircraft travels from V_{LOF} to the takeoff distance travelling at V_{TO} the following simple linear relationship was used, where the rotation time t_r of 3 seconds was used which was determined empirically relations by the size of the aircraft [17].

$$S_r = t_r V_{LOF} \quad (73)$$

The exact trajectory of the transition segment is greatly dependant on piloting technique. The radius of pull up in this segment R is given by equation (74), where V_{tr} is the transition velocity, and n is taken to be the load factor 1.2. As V_{tr} is $1.15V_s$ and g is the acceleration due to gravity, using equation (74) the radius of curvature R was then found. Once this was determined, equation(75) was used to calculate the climb angle.

$$R = \frac{(V_{tr})^2}{(n - 1)g} \quad (74)$$

$$\gamma_{cl} = \sin^{-1} \left(\frac{T_0}{W_0} - \frac{1}{D} \right) \quad (75)$$

$$h_{tr} = R(1 - \cos(\gamma)) \quad (76)$$

once these values were obtained, h_{tr} was obtained using equation(76).This value was then compared to h_{obs} and depending on which condition was satisfied for each of the three destinations, the values of S_{tr} and C_{cl} were determined. A summary of the parameters is found in the table below for all three destinations.

$$\text{if } h_{obs} \geq h_{tr} \quad S_{tr} = R \sin(\gamma_{cl}) \quad S_{cl} = \frac{h_{obs} - h_{tr}}{\tan \gamma_{cl}} \quad (77)$$

$$\text{if } h_{obs} < h_{tr} \quad S_{tr} = \sqrt{(R^2 - (R - h_{obs})^2)} \quad S_{cl} = 0 \quad (78)$$

Table 31: Breakdown of takeoff parameters

	Wellington	Christchurch	Hamilton
Distance(m)	Wet	Wet	Wet
S_g	702	623	544
S_r	216	241	234
S_{tr}	542	676	636
S_{cl}	0.00	0.00	0.00
S_{TO} (including safety factor in m)	1317	1286	1177

It can be clearly seen that for all three destinations the takeoff distance is well within the takeoff runway distance with the safety factor from FAR-25 conditions hence fulfilling the requirements.

13.2 Balanced Field Length

To account for the rare chance of engine failure, the balanced field length must be calculated. This distance is defined as the distance required by an aircraft to either continue takeoff and climb to the specific obstacle height or decelerate to a halt in the occasion of one engine inoperative. The following equation was used to calculate this value, where $G = \gamma_{cl} - \gamma_{min}$ and $\gamma_{min}=0.024$ as the aircraft consists of 2 engines [12], $U = 0.01 CL_{LOF} + 0.02$ the mean engine thrust for a turbofan during takeoff $\bar{T} = 0.75T_{takeoff-static}$ ($\frac{5+BPR}{4+BPR}$), and γ_{cl} is given by $\sin^{-1} [(\frac{N_e-1}{N_e}) (\frac{T_0}{W_0}) - \frac{D_{OEI}}{W_0}]$, where $N_e = 2$ as there are two engines. A summary of the parameters can be found in the table below.

$$BFL = \frac{0.863}{1 + 2.3G} \left(\frac{W/S}{\rho C_{L_{Climb}}} + h_{obs} \right) \left(\frac{1}{(\bar{T}/W) - U} + 2.7 + \frac{655}{\sqrt{\sigma}} \right) \quad (79)$$

The final values are summarised below.

Table 32: Breakdown of BFL parameters

	Wellington	Christchurch	Hamilton
Distance(m)	Wet	Wet	Wet
γ_{cl}	0.27	0.27	0.27
$T_0(KN)$	70.3	70.3	70.3
BPR	5.50	5.50	5.50
W_0	45887.9	45887.9	45887.9
$BFL(m)$	2208.141636	1968.067993	1735.148986

13.3 Landing Distance

The landing distance is calculated in a similar way to the takeoff distance. It is also composed of four key distances, which are the Approach, flare, rolling and braking distances. Again a safety factor of 1.66 must be applied according to FAR-25 restrictions. The total landing, therefore, becomes as shown below.

$$S_L = 1.666(S_a + S_f + S_{FR} + S_B) \quad (80)$$

The approach distance, S_a is calculated using equation(81) where $h_F = R(1-\cos(\gamma a))$ and $\gamma a = 3$ degrees [12]. Just like in the takeoff distance, the only difference in finding the value of R for the landing distance is that the velocity changes to V_F which is $1.23V_s$. n is again 1.2, and h_{obs} remains the same as before. using these values, the flare distance, S_f was also calculated using equation(82).

$$S_a = \frac{h_{obs} - h_F}{\tan(\gamma a)} \quad (81)$$

$$S_f = R \sin y_a \quad (82)$$

The final segment is the deceleration from V_{TD} to a standstill. The ground distance S_B is given by equation(83), where v_2 is the final velocity when the plane is stationary and $V_1 = V_{TD}$ which is 1.3 V_{stall} , where k_A and K_T are calculated using the same equation previously, with changed according to thrust and landing weights.

$$S_B = \frac{1}{k_A 2g} \ln \left(\frac{K_T + K_A V_2^2}{k_T + K_A V_1^2} \right) \quad (83)$$

A summary of the landing conditions are shown in the table below. The table outlines the landing distance for all 3 locations in both dry and wet conditions.

Table 33: Breakdown of landing parameters

	Wellington	Christchurch	Hamilton
Distance(m)	Wet	Wet	Wet
S_a	130.97	113.04	118.36
S_f	145.28	181.15	170.51
S_{td}	207	231.15	224.25
S_b	1012.45	1300.00	1218.812
S_L (including safety factor in m)	2492.74	3042.98	2888.44

13.4 Mission Performance

Table[34] show the updated aircraft range and endurance with the weight fraction, SFC, L/D_{cruise} updated with altitude and thrust corrections. Equation (84) [40] was used to calculate SFC with $c' = 0.7$ for large subsonic turbofans, BPR was the bypass ratio of 5.5 and M_N was the cruising Mach number. As discussed before, the fuel weight was increased to compensate for the lower L/D_{cruise} values. To calculate the W_i/W_{i-1} , there are 3 unknown weight fractions with one equation. Therefore, evaluating all segments bar one and determining if it satisfies the last segment requirement.

$$SFC = c'(1 - 0.15BPR^{0.65})[1 + 0.28(1 + 0.063BPR^2)M_N] \quad (84)$$

Table 34: Brequet Range/Endurance Updated

Flight Phase	Cruise 1	Cruise 2	Cruise 3	Diversion	Loiter
Stage M	0.690	0.645	0.667	0.690	NA
Alt(ft)	25000	30000	27500	25000	NA
SFC (hr^{-1})	0.559	0.538	0.549	0.559	0.470
$(L/D)_{Cruise}$	14.8	14.5	14.8	14.8	15.1
W_i/W_{i-1}	0.9816	0.9625	0.9754	0.9782	0.9770
Range/Endurance	477km	726km	437km	474km	45.0 min

Figure[28] illustrates how the range of the aircraft changes with changing payload. At the Maximum Zero Fuel Weight (MFZW), the aircraft has a range of 1.48×10^3 km. Keeping MTOW the same but decreasing the payload weight to account for reserve fuel gave a range of 2.41×10^3 km. This is the maximum amount of fuel the aircraft can take and means 2 passengers carrying their luggage are unable to be on the aircraft. In the scenario where the payload weight is just the 2 pilots weight 150 kg under FAR 25 regulations and the maximum range comes to 6.61×10^3 km.

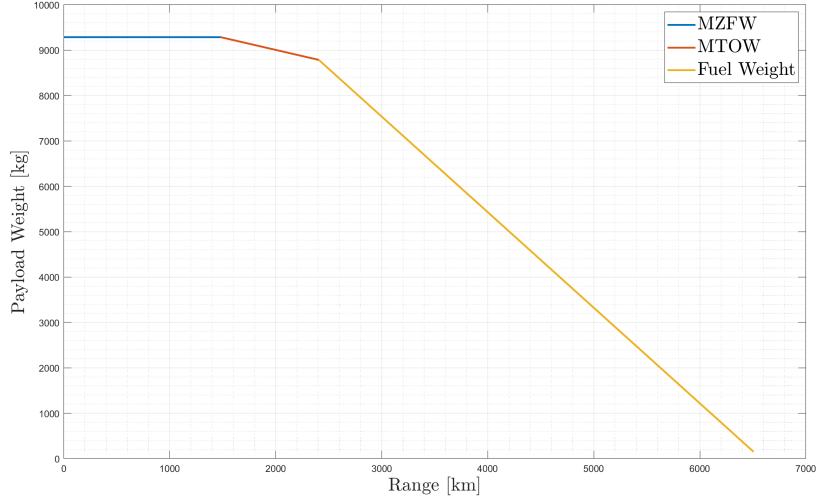


Figure 28: Range in range with different layout weight

13.5 Point Performance

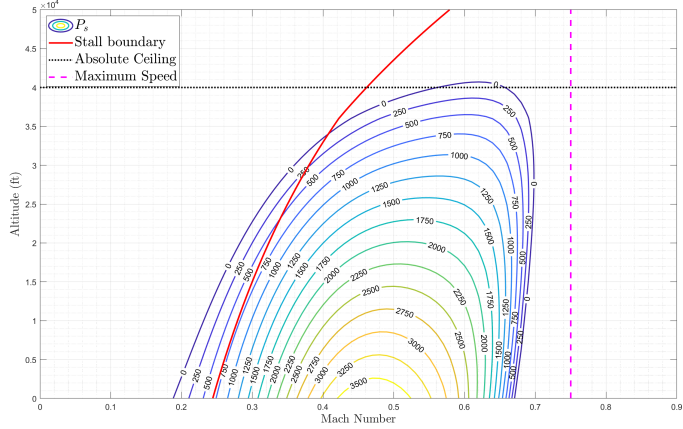


Figure 29: Specific Excess Power plot with the climb rate measured in ft/min

Equation(85) was used to calculate the specific excess thrust, P_s . Thrust lapse was implemented into the equation(86) provided by Howe[40] where σ was the density ratio using the ISA table, s was the exponent dependent on BPR which gave a value of 0.7. Lastly K_1 through K_4 were constants given in Table 3.2 in [40]. Drag was calculated using the coefficient of drag which was the summation of lift-induced drag, wave drag and form drag. Weight was taken to be MTOW and flight velocity V was be derived from M and the local speed of sound. Figure[29] show the P_s plot at the start of a cruise with MTOW. Stalling line and the maximum speed line was also plotted to give a better idea of which region the aircraft will be operating at. The absolute ceiling at 40000ft has been met However, the maximum speed the aircraft is able to reach is 0.7, falling behind of design maximum Mach number of 0.75. Reasons for the shortfall will be discussed further on in the design evaluation.

$$P_s = V \left(\frac{T - D}{W} \right) \quad (85)$$

$$T = \tau T_0 = T_0 (K_1 + BPR * K_2 + M(K_3 + BPR * K_4)) \sigma^s \quad (86)$$

14 Evaluation of Conceptual Design

The aircraft has mostly met the design requirements that satisfy with FAR 25 regulations. Given the conditions the design constraints gave, the aircraft can be trimmed without large trimming angles and the aircraft was stable for all three runs with static margin ranging from 11.4% to 12.6%.

However, there are areas for improvement. One of the largest drawbacks is the aircraft's inability to reach Mach 0.75 and at Mach 0.69, the throttle will be almost at 100%. A reason for it is that the initial C_{D_0} of 0.017 was extremely ambitious and the design was unable to reach the point. In conjunction with the thrust lapse equation which severely decreased the thrust at higher altitudes mean the design requirement was not met. A shorter fuselage and better nose design could reduce the C_{D_0} to enable the aircraft to reach higher speeds. An easier solution would be installing engines which produced more thrust and given the recalculated empty weight was 2 tonnes than initially conceived but that would entail the undercarriage, fuselage and possibly a wing redesign.

Another parameter that fell short of the initial choice was the L/D ratio. Again, the initial L/D ratio was very ambitious. One way to increase L/D is by decreasing C_{D_O} with the suggestion listed above for the next design iteration. Oswald efficiency can also be increased to obtain higher L/D with the effect of decreasing induced drag. Since the wing twist distribution was considered linear since there are no suitable methods to analyse the optimum twist distribution during the conceptual stage. However, this is not ideal and in the design stage, possible computational methods would be required to find an optimum wing twist distribution thus increasing the Oswald efficiency factor.

Another design consideration that fell short of the design constraint is the distance for balance field length and landing is far too long for all three runways. This and the SEP curve, suggest that the chosen design point was not suitable and it is obvious that the aircraft could not meet the landing constraints. The reason for placing the design point where it is was that the wing loading during the first was assumed to be ideal and so the design point was placed there. Placing the design point where the first takeoff and landing met would've solved the landing issue and with the increase in the thrust-to-weight ratio, it would have solved the lack of thrust as well. This would entail designing a whole new aircraft.

Winglets were not considered in the design since there was no good way to see the effect of winglets on the lift distribution since it shifts towards the tip of the wing. Consequently, the taper and twist alongside winglets to approximate an elliptical lift distribution would be unknown. Therefore, later in the design stage, winglets can be considered.

Given that the aircraft would not meet the majority of the field performance, the aircraft performed relatively well stability-wise, and the overestimating for the empty weight allowed extra fuel weight in order to reach the mission profile. The three-view drawing can be found in APPENDIX A.

References

- [1] Spreemann KP. DESIGN GUIDE FOR PITCH-UP EVALUATION AND INVESTIGATION AT HIGH SUBSONIC SPEEDS OF POSSIBLE LIMITATIONS DUE TO WING-ASPECT-RATIO VARIATIONS; 1961. <https://core.ac.uk/download/pdf/286871313.pdf>.
- [2] Torenbeek E. Design for performance. In: Synthesis of Subsonic Airplane Design. Springer; 1982. p. 141-80.
- [3] Abbott IH, Von Doenhoff AE. Theory of wing sections: including a summary of airfoil data. Courier Corporation; 2012.
- [4] Gudmundsson S. General Aviation Aircraft Design Applied Methods and Procedures. Second edition. ed. Amsterdam: Butterworth-Heinemann; 2021.
- [5] Sadraey MH. Aircraft Design: A Systems Engineering Approach; 2013.
- [6] Skinn D, Miedlar P, Kelly L. Flight Loads Data for a Boeing 737-400 in Commercial Operation. DAYTON UNIV OH RESEARCH INST; 1996.
- [7] Scholz D. Aircraft Design - an open educational resource (OER) for Hamburg Open Online University (HOOU). amburg Open Online University; 2020. <https://www.fzt.hawhamburg.de/pers/Scholz/HOOU/>.
- [8] Levis E. Flying Surface Design Slides. Department of Aeronautics; 2022.
- [9] Shortal JA, Maggin B. Effect of sweepback and aspect ratio on longitudinal stability characteristics of wings at low speeds - NASA technical reports server (NTRS). NASA; 1981. <https://ntrs.nasa.gov/citations/19930087879>.
- [10] Raymer DP. Aircraft Design: A Conceptual Approach. No. v. 1 in AIAA education series. American Institute of Aeronautics and Astronautics; 2006. Available from: <https://books.google.co.uk/books?id=bvxllgEACAAJ>.
- [11] Roskam J. Airplane Design: Part 2-Preliminary Configuration Design and Integration of the Propulsion System. DARcorporation; 1985.
- [12] Cross L. Propfan Power: The Story of the Unducted Fan Engine — airwaysmag.com; 2022. [Accessed 01-Dec-2022]. <https://airwaysmag.com/the-unducted-fan-engine/>.
- [13] Smithsonian. General Electric GE36 Unducted Fan (UDF) Turboprop Engine; 2022. [Accessed 01-Dec-2022]. https://airandspace.si.edu/collection-objects/general-electric-ge36-unducted-fan-udf-turboprop-engine/nasm_A19920001000.
- [14] Roskam J. Methods for Estimating Drag Polars of Subsonic Airplanes. Roskam Aviation and Engineering Corporation; 1971.
- [15] Aviation G. CF34-8C Turbofan Propulsion System Spec Sheet; 2020. [Accessed 30-Nov-2022]. <https://www.geaerospace.com/>.
- [16] LP ST. Tay 620 / 650 Power for the Fokker 70 / 100; 2004. [Accessed 30-Nov-2022]. https://myaeroengine.com/onwingcare/documents/tay_620_650_tcm92-5751.pdf.
- [17] Design Organisation E. Type-certificate data sheet - european union aviation safety agency; 2019. [Accessed 30-Nov-2022]. Available from: <https://www.easa.europa.eu/en/downloads/7767/en>.
- [18] Design Organisation E. European Union Aviation Safety Agency; 2022. [Accessed 30-Nov-2022]. Available from: <https://www.easa.europa.eu/en/downloads/33453/en>.
- [19] Design Organisation E. TYPE-CERTIFICATE DATA SHEET for SaM146 series engines; 2022. [Accessed 30-Nov-2022]. Available from: <https://www.easa.europa.eu/en/downloads/7737/en>.
- [20] Karnozov V. Aviadvgivatel Mulls Higher-thrust PD-14s To Replace PS-90A — ainonline.com; 2010. [Accessed 01-Dec-2022]. <https://www.ainonline.com/aviation-news/air-transport/2019-08-19/aviadvigatel-mulls-higher-thrust-pd-14s-replace-ps-90a>.
- [21] Kundu AK. Aircraft design. vol. 27. Cambridge University Press; 2010.
- [22] Mabanaft. Jet A-1 - Fuel Specification and Safety Data Sheet; 2022. [Accessed 30-Nov-2022]. <https://www.mabanaft.co.uk/products/jet-a-1>.
- [23] Van Den Bossche D. The A380 flight control electrohydrostatic actuators, achievements and lessons learnt. In: 25th international congress of the aeronautical sciences. International Council of Aeronautical Sciences (ICAS) Hamburg, Germany; 2006. p. 1-8.

- [24] Roskam J. Airplane Design: Part IV: Layout of Landing Gear and Systems. DAR Corporation; 2004.
- [25] Levis E. Weight Balance Estimation for Transport Aircraft. Department of Aeronautics; 2022.
- [26] Levis E. Undercarriage Layout and design. Department of Aeronautics; 2022.
- [27] Raymer DP. Aircraft Design: A Conceptual Approach. American Institute of Aeronautics and Astronautics; 2018.
- [28] Goodyear aviation. The Goodyear Tire amp; Rubber Company; 2022. Available from: <https://www.goodyearaviation.com/resources/pdf/Aviation-Databook-2022.pdf>.
- [29] Anonym. COMFAA 3.0. Federal Aviation Administration; 2021. Available from: <https://www.airporttech.tc.faa.gov/Products/Airport-Safety-Papers-Publications/Airport-Safety-Detail/ArtMID/3682/ArticleID/10/COMFAA-30>.
- [30] Raymer DP. Aircraft Design: A Conceptual Approach. American Institute of Aeronautics and Astronautics; 2018.
- [31] Perkins CD, Hage RE, Perkins D, Hage RE. Airplane performance, stability and control. John Wiley & Sons Incorporated; 1949.
- [32] Levis E. Aerodynamics Slides. Department of Aeronautics; 2022.
- [33] Schlichting H, Kestin J. Boundary layer theory. vol. 121. Springer; 1961.
- [34] Nicolai LM. Fundamentals of aircraft design. Nicolai; 1975.
- [35] Sforza PM. Commercial airplane design principles. Elsevier; 2014.
- [36] Gilruth R, White M. Analysis and prediction of longitudinal stability of airplanes. US Government Printing Office; 1941.
- [37] Levis E. Stability Slides. Department of Aeronautics; 2022.
- [38] Mason W. Transonic Aerodynamics of airfoils and wings. Notes in Configuration Aerodynamics, Virginia Tech. 2006;4(4):02.
- [39] Cook MV. Flight Dynamics Principles: A Linear Systems Approach to Aircraft Stability and Sontrol. Butterworth-Heinemann; 2012.
- [40] Howe D, Rorie G. Aircraft Conceptual Design Synthesis. Professional Engineering Publishing London, UK; 2000.

Appendix

A Appendix: Three View Drawing

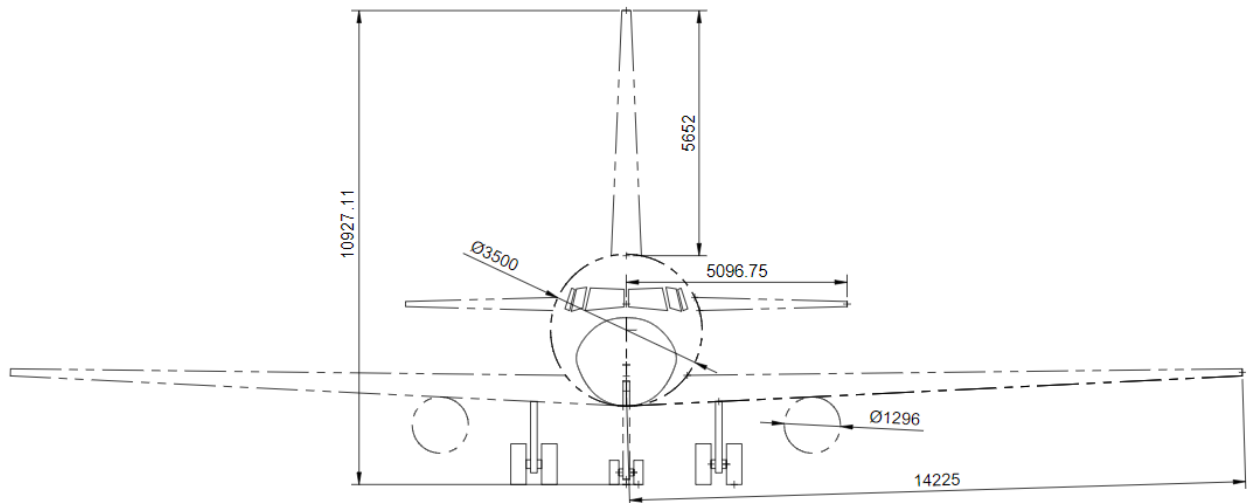


Figure 30: Front View

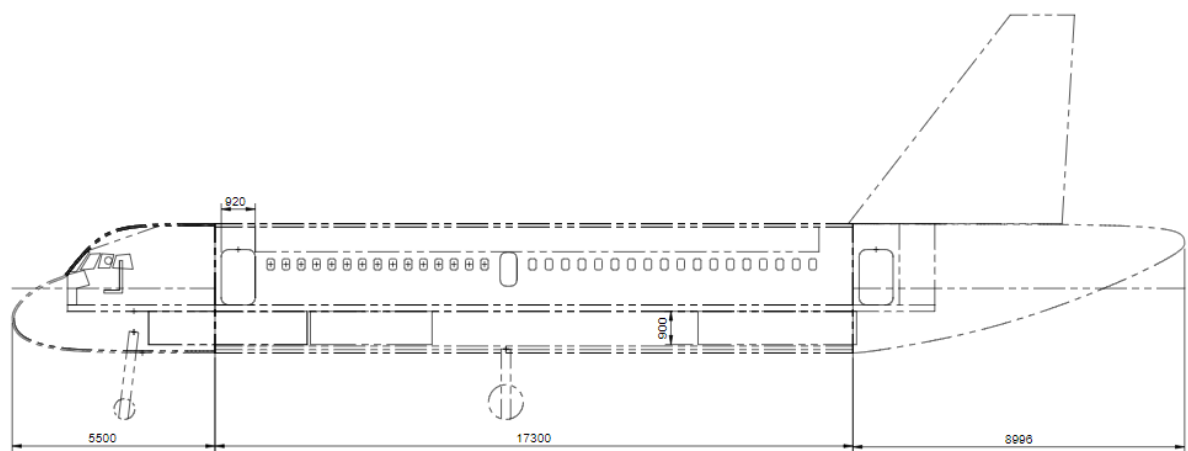


Figure 31: Side View

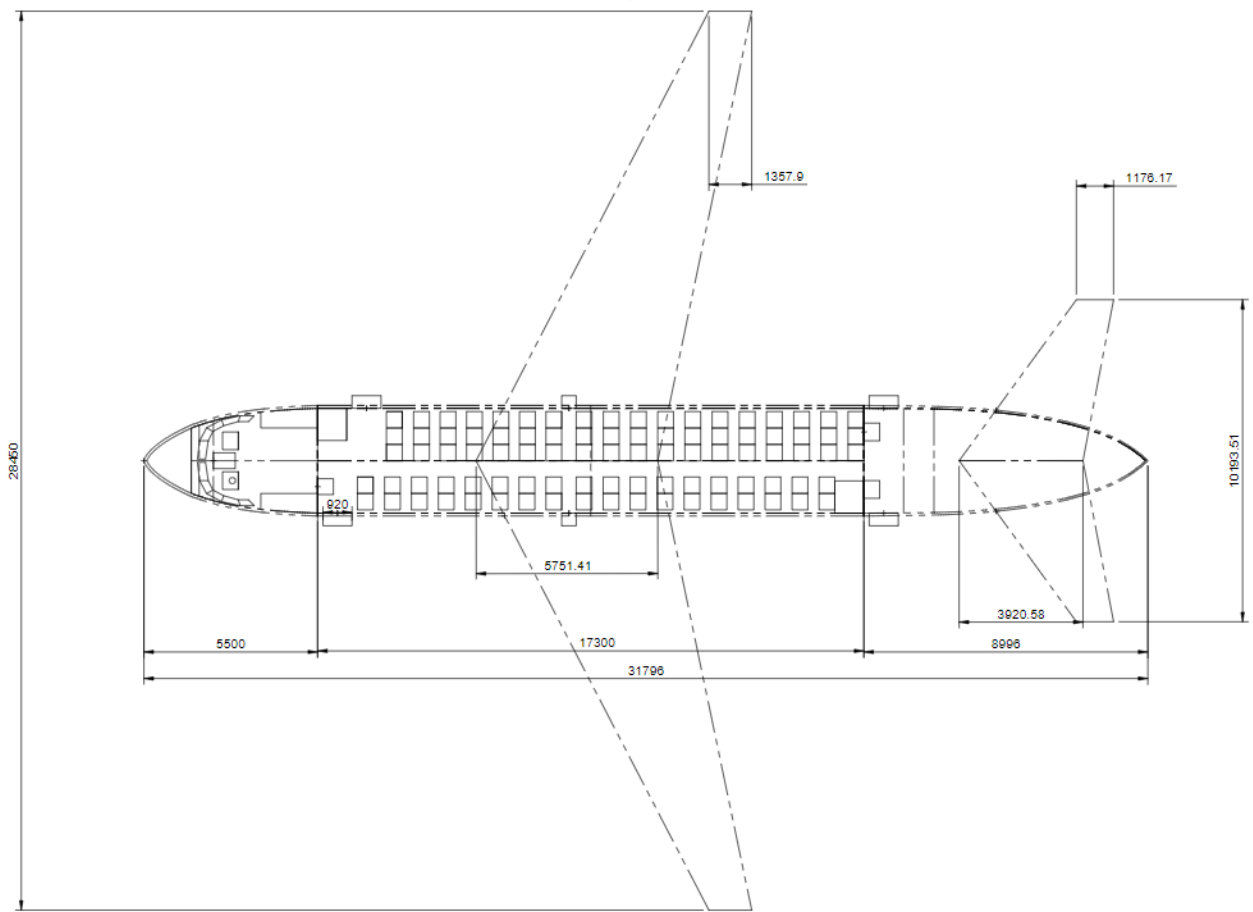


Figure 32: Top View

B Appendix: Poster Design

Imperial College London **Department of AERONAUTICS**

Conceptual Design for a Regional Jet Aircraft

Group 1: Avish (Ave) Madhow, Stephen Cao, Aryaa Desai, YiChen You, Amelia Samuel, Chris Ziyi Yao

DESIGN SPECIFICATION																																																					
<p>MISSION PROFILE</p>	<p>DESIGN CONSTRAINTS</p> <ul style="list-style-type: none"> 90 passengers and baggage. 2 pilots and 3 cabin crew. 30 minute turnaround at each location with powerplant idling: no refuelling. Diversion and 45 minute loiter at 5000 ft Absolute ceiling: 40,000 ft Maximum speed of Mach 0.75 Compliant with FAR-25 regulations. 																																																				
BASELINE CONFIGURATION																																																					
<p>LOW WING</p> <ul style="list-style-type: none"> Easy cabin access. Shortened take-off distance due to enhanced ground effect and softer touchdown. Reduced impact of downwash from wings on horizontal stabiliser. <p>UNDERWING ENGINES</p> <ul style="list-style-type: none"> High bypass turbofan engines. Minimise interference drag. Easy to service: minimal extra equipment required and faster turnaround. <p>TRICYCLE UNDERCARRIAGE</p> <ul style="list-style-type: none"> Front wheel enables steering and prevents tipping in the event of harsh braking. Stored underwing for better aerodynamics. 	<p>CONVENTIONAL TAIL</p> <ul style="list-style-type: none"> Lightweight: no additional reinforcement needed. Good indication when stall is near: violently vibrates when approaching stall. <p>HIGH LIFT DEVICES</p> <ul style="list-style-type: none"> Fowler flaps: Increase $C_{L_{max}}$ Easily maintained Reliable activation mechanism <p>Slats:</p> <ul style="list-style-type: none"> Increase $C_{L_{max}}$ 																																																				
INITIAL SIZING																																																					
<p>Figure 1: Weight Fractions</p> <p>Table 1: Weight Fraction Estimations</p> <table border="1"> <thead> <tr> <th>Journey Segments</th> <th>Weight Fractions</th> </tr> </thead> <tbody> <tr> <td>S1: Wellington – Christchurch</td> <td>0.918</td> </tr> <tr> <td>S2: Christchurch – Hamilton</td> <td>0.834</td> </tr> <tr> <td>S3: Hamilton – Wellington</td> <td>0.767</td> </tr> <tr> <td>D: Hamilton – Wellington (including diversion)</td> <td>0.734</td> </tr> </tbody> </table> <p>Fuel: 27% Crew and Passengers: 15% Payload: 7% Empty: 51%</p>	Journey Segments	Weight Fractions	S1: Wellington – Christchurch	0.918	S2: Christchurch – Hamilton	0.834	S3: Hamilton – Wellington	0.767	D: Hamilton – Wellington (including diversion)	0.734	<p>Initial guesses of $AR = 8$, $S_{ref}/S_{wet} = 5.5$ and $e = 0.8$ were made.</p> <p>$\left(\frac{T}{W}\right)_{max}$ and C_{D_0} calculated using $\left(\frac{T}{W}\right)_{max} = \frac{1}{2} \sqrt{\frac{\pi AR e}{C_{D_0}}} = K_{LD} \frac{AR}{S_{ref}} \cdot [4]$</p> <p>Weight fractions for specific flight segments make use of [4]:</p> <ul style="list-style-type: none"> Specific Fuel Consumption: $C_{specific} = 1.38 \times 10^{-4} s^{-1}$, $C_{loiter} = 1.11 \times 10^{-4} s^{-1}$. Range constraints: $\frac{W_t}{W_{t-1}} = e^{\frac{-\int \frac{1}{W} dS}{AR}}$. Endurance constraints: $\frac{W_t}{W_{t-1}} = e^{\frac{-\int \frac{1}{W} dS}{eC}}$. <p>Fuel weight fraction: $\frac{W_f}{W_0} = 1.01 \left(1 - \frac{W_e}{W_0}\right)$, where $\frac{W_e}{W_0} = \frac{W_e}{W_{t-1}} * ... * \frac{W_1}{W_0}$.</p> <p>Empty weight fraction: $\frac{W_e}{W_0} = AW_0^C$, where $A = 0.97$ and $C = -0.06$. [1]</p> <p>Iterative equation based on initial W_0 guess : $W_0 = \frac{W_{crew} + W_{payload}}{1 - \left(\frac{W_f}{W_0} + \frac{W_e}{W_0}\right)}$.</p>																																										
Journey Segments	Weight Fractions																																																				
S1: Wellington – Christchurch	0.918																																																				
S2: Christchurch – Hamilton	0.834																																																				
S3: Hamilton – Wellington	0.767																																																				
D: Hamilton – Wellington (including diversion)	0.734																																																				
SIZING TO CONSTRAINT																																																					
<p>Figure 2: Final Constraint Diagram</p> <p>FIELD PERFORMANCE: Empirical formulae shown below are used to calculate T/O & landing distances.</p> <p>Table 2: Design Process for Field Performance</p> <table border="1"> <thead> <tr> <th>Segment</th> <th>Formula used [3]</th> <th>Constraints</th> <th>$C_{L_{max}}$ and V [2]</th> </tr> </thead> <tbody> <tr> <td>Take-off</td> <td>$TOP = \frac{W_0/S}{(T/W)\sigma C_{L_{max,T0}}}$</td> <td>$TOP_1 = 9576 N/m^2$ $TOP_2 = 13885 N/m^2$ $TOP_3 = 9097 N/m^2$</td> <td>$C_{L_{max,T0}} = 2.1$ $V_{TO} = 1.1V_S$</td> </tr> <tr> <td>Landing / Approach</td> <td>$ALD = \frac{0.51W/S}{\sigma C_{L_{max,L}}}$</td> <td>$ALD = \frac{3}{5} * LDA$</td> <td>$C_{L_{max,L}} = 3.3$ $\Delta C_{L_{max,HLD}} = 1.7$ $V_A = 1.3V_S$</td> </tr> </tbody> </table> <p>Table 4: Final results at chosen design point</p> <table border="1"> <thead> <tr> <th>W_0/S_{ref}</th> <th>S_{ref}</th> <th>T_0/W_0</th> <th>W_0</th> <th>AR</th> <th>e</th> <th>S_{wet}/S_{ref}</th> <th>C_{D_0}</th> <th>W_e/W_0</th> <th>W_f/W_0</th> <th>$\left(\frac{T}{W}\right)_{max}$</th> <th>$K_{LD}$</th> <th>MAX Range</th> <th>MAX Endurance</th> </tr> </thead> <tbody> <tr> <td>4160 N/m²</td> <td>113.87 m²</td> <td>0.246</td> <td>48288 kg</td> <td>8</td> <td>0.8</td> <td>5.007</td> <td>0.0262</td> <td>0.508</td> <td>0.269</td> <td>19.6</td> <td>15.5</td> <td>7570 km</td> <td>9.06 hrs</td> </tr> </tbody> </table>	Segment	Formula used [3]	Constraints	$C_{L_{max}}$ and V [2]	Take-off	$TOP = \frac{W_0/S}{(T/W)\sigma C_{L_{max,T0}}}$	$TOP_1 = 9576 N/m^2$ $TOP_2 = 13885 N/m^2$ $TOP_3 = 9097 N/m^2$	$C_{L_{max,T0}} = 2.1$ $V_{TO} = 1.1V_S$	Landing / Approach	$ALD = \frac{0.51W/S}{\sigma C_{L_{max,L}}}$	$ALD = \frac{3}{5} * LDA$	$C_{L_{max,L}} = 3.3$ $\Delta C_{L_{max,HLD}} = 1.7$ $V_A = 1.3V_S$	W_0/S_{ref}	S_{ref}	T_0/W_0	W_0	AR	e	S_{wet}/S_{ref}	C_{D_0}	W_e/W_0	W_f/W_0	$\left(\frac{T}{W}\right)_{max}$	K_{LD}	MAX Range	MAX Endurance	4160 N/m ²	113.87 m ²	0.246	48288 kg	8	0.8	5.007	0.0262	0.508	0.269	19.6	15.5	7570 km	9.06 hrs	<p>POINT PERFORMANCE: Using the Specific Excess Power [3] equation at ISA conditions, all point performances were determined except for absolute ceiling.</p> $\left(\frac{T}{W}\right)_0 = \frac{a}{\beta} \left(\frac{1}{V_\infty} \frac{dh}{dt} + \frac{1}{g} \frac{dv_\infty}{dt} + \frac{\frac{1}{2} \rho V_\infty^2 C_D}{\alpha S_{ref}} + \frac{\alpha n^2 \frac{W_0}{S_{ref}}}{\frac{1}{2} \rho V_\infty^2 n AR e} \right) [3]$ <p>Table 3: Design Process for Point Performance</p> <table border="1"> <thead> <tr> <th>Mission Segment</th> <th>Reasoning and Parameters</th> <th>Assumptions</th> </tr> </thead> <tbody> <tr> <td>Take-off and Landing Climb</td> <td>Take-off climb for twin-engines consists of 3 stages, subjected to minimum climb gradients, dh/dt, of 0%, 2.4% and 1.2% respectively.[5] Similarly, landing climb (AEO) and approach climb (OEI) require dh/dt of 3.2% and 2.1% respectively.[5]</td> <td> <ul style="list-style-type: none"> Instantaneous climb assumed such that the aircraft only operates at minimum climb gradient. Negligible ground effects. </td> </tr> <tr> <td>Cruise</td> <td>Cruise 1 performed at 25,000 ft as per requirements. Cruise 2 and 3 performed at 36,000 ft from typical values of similar aircraft. $C_{L_{max}}$ (clean configuration) = 1.9</td> <td> <ul style="list-style-type: none"> Steady level flight. Cruise 1 performed at Mach 0.69. Cruise 2 & 3 performed at maximum speed of Mach 0.75 (to present the most constraining situation). </td> </tr> <tr> <td>Absolute Ceiling</td> <td>Absolute ceiling is at 40,000 ft. Since $T = D_{min}/W$ at steady level flight, using: $\frac{T_0}{W} = \frac{D_{min}}{W} \frac{1}{1.439 \sigma \left(\frac{T}{W}\right)_{max}}$, $\left(\frac{T}{W}\right)_0$ for maximum ceiling is calculated.</td> <td> <ul style="list-style-type: none"> Max ceiling is reached during Cruise 2 and 3. $\left(\frac{T}{W}\right)_{max,cruise} = 0.866 \left(\frac{T}{W}\right)_{max}$ Clean configuration for aircraft assumed. </td> </tr> </tbody> </table> <p>[1] Daniel P. Raymer, <i>Aircraft Design: A Conceptual Approach</i>. American Institute of Aeronautics and Astronautics. 1992. [2] Dr. Jan Rookman, <i>Airplane Design Part 1: Preliminary sizing of airplanes</i>. Rockman Aviation and Engineering Corporation. 1985. [3] Dr. Ermikos Lewis, <i>Sizing to Constraints Lecture Notes</i>. Department of Aeronautics, Imperial College London. 2022. [4] Dr. Robert Hewson, <i>Initial Sizing Lecture Notes</i>. Department of Aeronautics, Imperial College London. 2022. [5] Part 25 Airworthiness Standards: Transport Category Airplanes, Code of Federal Regulations. 2022.</p>	Mission Segment	Reasoning and Parameters	Assumptions	Take-off and Landing Climb	Take-off climb for twin-engines consists of 3 stages, subjected to minimum climb gradients, dh/dt , of 0%, 2.4% and 1.2% respectively.[5] Similarly, landing climb (AEO) and approach climb (OEI) require dh/dt of 3.2% and 2.1% respectively.[5]	<ul style="list-style-type: none"> Instantaneous climb assumed such that the aircraft only operates at minimum climb gradient. Negligible ground effects. 	Cruise	Cruise 1 performed at 25,000 ft as per requirements. Cruise 2 and 3 performed at 36,000 ft from typical values of similar aircraft. $C_{L_{max}}$ (clean configuration) = 1.9	<ul style="list-style-type: none"> Steady level flight. Cruise 1 performed at Mach 0.69. Cruise 2 & 3 performed at maximum speed of Mach 0.75 (to present the most constraining situation). 	Absolute Ceiling	Absolute ceiling is at 40,000 ft. Since $T = D_{min}/W$ at steady level flight, using: $\frac{T_0}{W} = \frac{D_{min}}{W} \frac{1}{1.439 \sigma \left(\frac{T}{W}\right)_{max}}$, $\left(\frac{T}{W}\right)_0$ for maximum ceiling is calculated.	<ul style="list-style-type: none"> Max ceiling is reached during Cruise 2 and 3. $\left(\frac{T}{W}\right)_{max,cruise} = 0.866 \left(\frac{T}{W}\right)_{max}$ Clean configuration for aircraft assumed.
Segment	Formula used [3]	Constraints	$C_{L_{max}}$ and V [2]																																																		
Take-off	$TOP = \frac{W_0/S}{(T/W)\sigma C_{L_{max,T0}}}$	$TOP_1 = 9576 N/m^2$ $TOP_2 = 13885 N/m^2$ $TOP_3 = 9097 N/m^2$	$C_{L_{max,T0}} = 2.1$ $V_{TO} = 1.1V_S$																																																		
Landing / Approach	$ALD = \frac{0.51W/S}{\sigma C_{L_{max,L}}}$	$ALD = \frac{3}{5} * LDA$	$C_{L_{max,L}} = 3.3$ $\Delta C_{L_{max,HLD}} = 1.7$ $V_A = 1.3V_S$																																																		
W_0/S_{ref}	S_{ref}	T_0/W_0	W_0	AR	e	S_{wet}/S_{ref}	C_{D_0}	W_e/W_0	W_f/W_0	$\left(\frac{T}{W}\right)_{max}$	K_{LD}	MAX Range	MAX Endurance																																								
4160 N/m ²	113.87 m ²	0.246	48288 kg	8	0.8	5.007	0.0262	0.508	0.269	19.6	15.5	7570 km	9.06 hrs																																								
Mission Segment	Reasoning and Parameters	Assumptions																																																			
Take-off and Landing Climb	Take-off climb for twin-engines consists of 3 stages, subjected to minimum climb gradients, dh/dt , of 0%, 2.4% and 1.2% respectively.[5] Similarly, landing climb (AEO) and approach climb (OEI) require dh/dt of 3.2% and 2.1% respectively.[5]	<ul style="list-style-type: none"> Instantaneous climb assumed such that the aircraft only operates at minimum climb gradient. Negligible ground effects. 																																																			
Cruise	Cruise 1 performed at 25,000 ft as per requirements. Cruise 2 and 3 performed at 36,000 ft from typical values of similar aircraft. $C_{L_{max}}$ (clean configuration) = 1.9	<ul style="list-style-type: none"> Steady level flight. Cruise 1 performed at Mach 0.69. Cruise 2 & 3 performed at maximum speed of Mach 0.75 (to present the most constraining situation). 																																																			
Absolute Ceiling	Absolute ceiling is at 40,000 ft. Since $T = D_{min}/W$ at steady level flight, using: $\frac{T_0}{W} = \frac{D_{min}}{W} \frac{1}{1.439 \sigma \left(\frac{T}{W}\right)_{max}}$, $\left(\frac{T}{W}\right)_0$ for maximum ceiling is calculated.	<ul style="list-style-type: none"> Max ceiling is reached during Cruise 2 and 3. $\left(\frac{T}{W}\right)_{max,cruise} = 0.866 \left(\frac{T}{W}\right)_{max}$ Clean configuration for aircraft assumed. 																																																			

Figure 33: Initial Design Poster